AGU PUBLICATIONS

JGR

Journal of Geophysical Research: Oceans

RESEARCH ARTICLE

10.1002/2015JC011091

Key Points:
- Simulations reproduce observed seasonal shift in ocean structure in Nares Strait
- Shift tied to differing surface friction associated with mobile and landfast ice
- Distribution of heat and salt is systematically altered by the presence of ice

Correspondence to:
E. Shroyer,
eshroyer@coas.oregonstate.edu

Citation:
Shroyer, E. L., R. M. Samelson, L. Padman, and A. Münchow (2015), Modeled ocean circulation in Nares Strait and its dependence on landfast-ice cover, *J. Geophys. Res. Oceans*, *120*, doi:10.1002/2015JC011091.

Received 30 JUN 2015
Accepted 9 NOV 2015
Accepted article online 12 NOV 2015

Modeled ocean circulation in Nares Strait and its dependence on landfast-ice cover

Emily L. Shroyer[1], Roger M. Samelson[1], Laurie Padman[2], and Andreas Münchow[3]

[1]College of Earth, Ocean, and Atmospheric Sciences, Oregon State University, Corvallis, Oregon, USA, [2]Earth and Space Research, Corvallis, Oregon, USA, [3]College of Earth, Ocean, and Environment, University of Delaware, Newark, Delaware, USA

Abstract Two simplified ocean simulations are used to study circulation and transport within Nares Strait. The simulations are similar, except that one included a coupled sea ice model that effectively established a landfast ice cover throughout the simulation year. Comparison between the ocean-only and ocean-ice simulations reveals a systematic change in the current structure, reminiscent of the seasonal shift under mobile and landfast ice previously observed in Nares Strait. A surface-intensified jet, which carries low-salinity water along the strait's centerline, develops within the ocean-only simulation. The current structure under landfast ice is characterized by a subsurface jet located along the western side with low-salinity surface water distributed along the eastern side of the strait. Intermediate salinity water is offset to the west in the ice-ocean simulation relative to the ocean-only simulation, while high-salinity water ($>$34.8) is constrained to recirculations that are located north and south of a sill in Kane Basin. The simulations, combined with an idealized, semianalytical model, suggest that the structural shift is caused by the surface Ekman layer beneath the landfast ice and the associated eastward advection of near-surface low-salinity water and westward movement of the jet. Temporal variability in the ocean-ice simulation is dominated by the remote response to the time-dependent northern boundary conditions. In contrast, the ocean-only simulation favors an instability and additionally responds to local surface wind forcing, which enhances the variability within the strait above that imposed at the boundaries.

1. Introduction

Nares Strait (Figure 1) carries freshwater and heat between the Lincoln Sea of the Arctic Ocean and Baffin Bay to the south. The strait is bordered by Ellesmere Island to the west and Greenland to the east. Its width varies from roughly 20 km across Robeson Channel at its northern end to over 140 km across Kane Basin, which is located near the middle of the strait's 500 km length. Strong, generally southward winds are channeled along the strait by steep terrain that rises up 500–2000 m above sea level within approximately 5 km of the coastline [*Samelson and Barbour*, 2008]. Nares Strait transports roughly 0.7 Sv in volume and 25–30 mSv in liquid freshwater equivalent (relative to a reference salinity of 34.8) toward the Labrador Sea [*Münchow et al*., 2006; *Münchow and Melling*, 2008], equivalent to roughly one-third of the volume and liquid freshwater outflow through Davis Strait [*Beszczynska-Möller et al*., 2011; *Curry et al*., 2014]. The above estimates neglect near-surface water, which may contain as much as half of the total freshwater transport and roughly 20% of the volume transport [*Münchow*, 2015]. The total volume transport ranges from as much as 1.5 Sv to close to zero [*Münchow*, 2015], and its variability has been linked to fluctuations in the large-scale along channel pressure gradient [*Kliem and Greenberg*, 2003; *Münchow*, 2015]. In addition to liquid freshwater, Nares Strait seasonally transports an estimated 4–8 mSv of ice southward [*Kwok*, 2005; *Kwok et al*., 2010, assuming 4 m thick ice]. Ice conditions typically alternate between landfast and mobile states that are associated with the formation and breakdown of ice arches across Smith Sound and northern Robeson Channel [*Kwok et al*., 2010]. In years in which neither ice arch forms, such as 2007, ice fluxes roughly 2–3 times those of a typical year have been inferred [*Kwok et al*., 2010] and modeled [*Rasmussen et al*., 2010].

The multiyear Canadian Archipelago Throughflow Study [CATS; *Münchow and Melling*, 2008] maintained a mooring array across southern Kennedy Channel (roughly 80.5°N, Figure 1) from 2003 to 2012. These data have provided a wealth of information about the current structure and hydrographic conditions across Nares Strait, and the corresponding volume and freshwater fluxes. In the annual mean, flow across most of

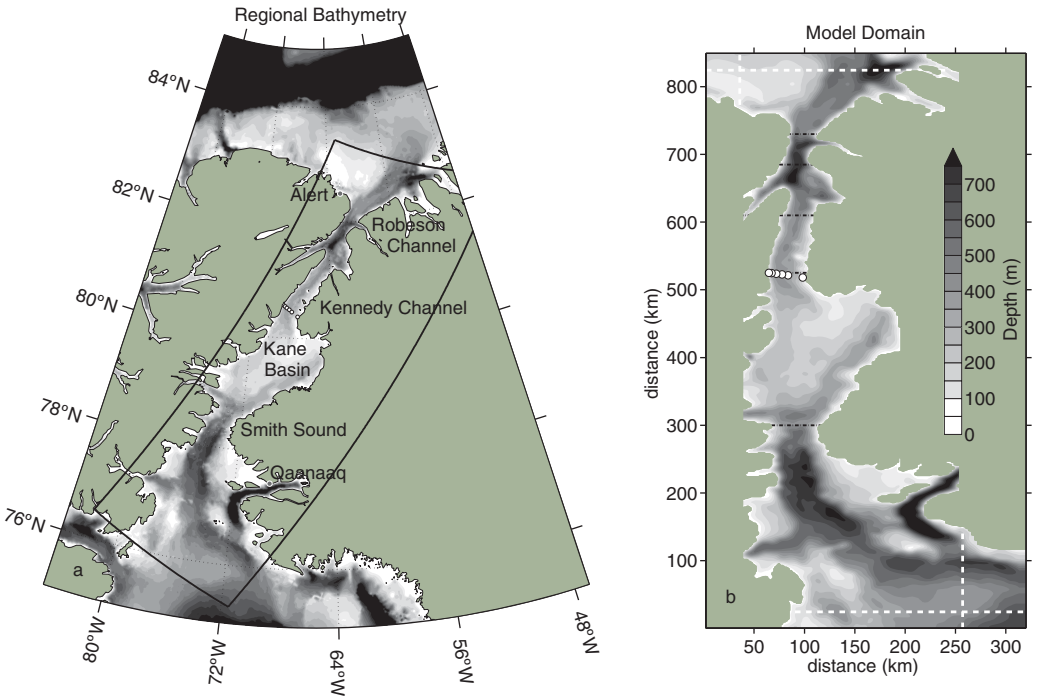

Figure 1. (a) Regional bathymetry and (b) model domain. White-dashed lines in Figure 1b indicate the extent of the sponge region, and black-dashed lines show the N. Robeson Channel, S. Robeson Channel, Kennedy Channel, CATS mooring, and Smith Sound transects. White circles show deployment locations of the CATS moorings.

Kennedy Channel is southward with a vertically averaged magnitude of about 7 cm s^{-1} on the western side of the channel. On the eastern edge of the channel (south of Franklin Island located at 80.8°N, 66.5°W), a narrow current heads to the north with a depth mean of roughly 4 cm s^{-1}. *Rabe et al*. [2012] showed that the mean structure of the main southward current is markedly different under landfast and mobile ice conditions, with important implications for seasonal and interannual variability of freshwater transport through the strait. A primary goal of this study is to provide a dynamical rationalization of this observed shift in current structure in southern Kennedy Channel, and to understand it in the wider context of flow through the full length of the strait.

In order to accomplish these objectives, two simplified models are used to examine and compare the along-strait evolution of the flow through Nares Strait under ice-free and landfast-ice conditions. We aim to extend our understanding of the current structure obtained through CATS to the entire strait spanning from Robeson Channel in the north to Smith Sound in the south (Figure1). First, we compare model results to the CATS observations, in order to illustrate the systematic differences in ocean circulation under varying ice conditions and to assess the extent to which the models reproduce the CATS observations. Second, we analyze the model circulation to determine the controlling dynamics and develop a rationalization for different circulation patterns under varying ice conditions, providing a simple, dynamical framework for the observed shift in current structure under mobile and landfast ice. This comparison provides a physical basis that should be useful for understanding not only the observed seasonal changes in the current structure, but also interannual variability within Nares Strait associated with changes in sea ice conditions (e.g., the 2007 ice flux anomaly). These results could also provide a benchmark for determining shifts in circulation under a changing climate (with the assumption of less landfast ice cover under warming conditions).

Because of Nares Strait's role in Arctic freshwater and volume budgets, factors determining the transport within the strait have been the focus of several regional-scale ocean models. These efforts include multidecadal large-scale (pan-Arctic to global), eddy-resolving models [*Lique et al*., 2009; *Aksenov et al*., 2010; *McGeehan and Maslowski*, 2012; *Lu et al*., 2014], and unstructured mesh models with refinement in the Arctic [*Wekerle et al*., 2013]. Most of these studies show a strong correlation between volume transport within Nares Strait and the sea surface height (SSH) gradient between the Arctic and Baffin Bay. *McGeehan and*

Maslowski [2012] estimate that roughly half of the variability in SSH is set by changes in the downstream and theorize that this variability is related to changes in transport of the West Greenland Current, while *Lu et al*. [2014] find a seasonality to the relative importance of upstream and downstream changes in SSH with the former taking a larger role in spring and summer. *Wekerle et al*. [2013] further suggest that upstream variability in SSH is linked to changes in wind regimes and export of freshwater from the Beaufort Gyre, while downstream variability in SSH is linked to air-sea fluxes in Baffin Bay and the Labrador Sea. Although these efforts have helped clarify the larger-scale factors that set the total freshwater and volume transports, the intent of the present study is to improve understanding of the detailed dynamics that control the distribution of heat and salinity within the strait. Developing this understanding is a necessary step toward predicting regional responses to future or past scenarios, which may in turn have broader implications. For example, the heat and freshwater budgets within the fjord determine access to heat and salt within the marine-terminating glacial fjords that open onto the strait [e.g., *Rignot et al*., 2012; *Straneo and Heimbach*, 2013]—factors that may be a significant contributor to recent mass loss of the Greenland ice sheet [*Enderlin et al*., 2014].

This work builds upon and extends previous regional modeling studies of Nares Strait, which have focused primarily on the dynamics of seasonal evolution of sea ice cover within the strait [*Rasmussen et al*., 2010] and ice arch formation [*Dumont et al*., 2009], rather than the baroclinic structure of the associated ocean circulation. The complementary approach taken here uses a simplified representation of sea ice variability, and focuses instead on the ocean circulation dynamics and its dependence on the presence or absence of sea ice. Accurate modeling of sea ice variability and seasonality in Nares Strait remains a challenge, as relevant processes such as the establishment and maintenance of ice arches are sensitive to sea ice rheology, ocean currents and heat transports, wind forcing, and other factors. The present study, which purposely minimizes consideration of the complexities of the sea ice dynamics, is intended as one step toward the long-term goal of a comprehensive understanding of coupled ocean and ice dynamics in Nares Strait and their influence on Arctic-Subarctic exchange.

2. Model Setup and Forcing

A regional model of Nares Strait was configured using a hydrostatic primitive-equation general circulation model [MITgcm; *Marshall et al*., 1997] on a staggered C-grid with height coordinates and shaved bottom cells [*Adcroft et al*., 1997]. The model domain (Figure 1) was divided into 200 by 680 rectilinear grid cells with 27 vertical levels. A constant horizontal grid spacing of 1.25 km was used in the nominal along-strait direction; the grid spacing varied from roughly 0.75–3.5 km in the nominal across-strait direction with the finest resolution located midstrait. The vertical spacing varied from 15 m in the upper 150–50 m below 400 m. Model bathymetry was created from the International Bathymetric Chart of the Arctic Ocean version 3.0 [*Jakobsson et al*., 2012]. The maximum depth was capped at 750 m for computational convenience; within Nares Strait, this cap influences only a small region near Petermann Fjord.

The model implementation used a nonlinear equation of state from *Jackett and McDougall* [1995] and the KPP vertical mixing scheme [*Large et al*., 1994] with background diffusivity and viscosity set to 10^{-5} m^2s^{-1}. The explicit horizontal diffusivity was set to zero, and the horizontal viscosity varied according to the grid size from roughly 10 m^2s^{-1} to 40 m^2s^{-1}. A free slip condition was applied at the horizontal ocean boundary. The bottom stress was formulated as a quadratic drag law with coefficient $C_D = 0.002$.

Initial fields and boundary conditions were taken from daily average fields of the nontidal Naval Research Laboratory's HYbrid Coordinate Ocean Model and Navy Coupled Ocean Data Assimilation Global $1/12^\circ$ analysis (HYCOM + NCODA) [*Chassignet et al*., 2007; *Metzger et al*., 2014]. Open-boundary conditions were implemented using a relaxation term added to momentum and tracer equations over a 20 cell sponge layer. The restoring time scale increased linearly from 3 h at the boundary to 3 days at a distance of 20 cells from the boundary. HYCOM + NCODA fields were linearly interpolated onto the regional grid. The net incoming volume transport was balanced by applying a uniform adjustment at each time step to normal velocity fields at the eastern and southern open boundaries. To reduce model bias, a depth-dependent correction to the HYCOM temperature and salinity fields was applied uniformly in time and the horizontal, to both the open boundary conditions and the initial fields. The temperature correction varied from 0°C above 150 m to 0.25°C below 200 m with a smooth transition between these depth ranges; the salinity correction

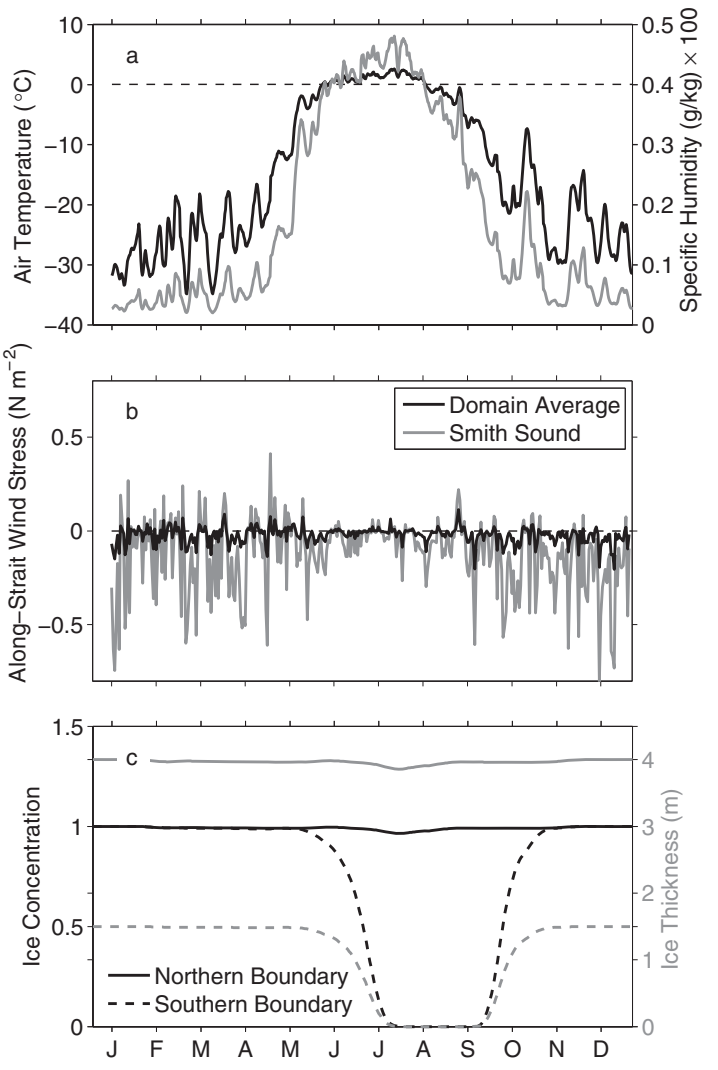

Figure 2. Model forcing time series and boundary fields showing (a) atmospheric temperature (black) and specific humidity (gray), (b) the along-strait wind stress (domain mean in black and a point near Smith Sound in gray), and (c) ice concentration (black, LHS), and ice thickness (gray, RHS) at the northern (solid) and southern boundaries (dashed). Sea ice fields along the western and eastern boundary are linearly interpolated between the north and the south.

varied smoothly from 0 at the surface to 1 below 300 m depth. Bias corrections were determined by comparing annual and across-strait mean fields from a noncorrected simulation to the observed fields.

Surface winds have systematic spatial variations related to the strait's orography [*Samelson and Barbour*, 2008]. To capture the effect of these features, spatially variable winds from a high-resolution regional atmospheric model of Nares Strait [*Samelson and Barbour*, 2008] were linearly interpolated in space and time from the mesoscale model's 3 hourly, 6 km grid wind fields to the ocean model grid and three-minute time step (Figure 2b). Atmospheric temperature and humidity fields, on the other hand, were taken to be spatially uniform, in order to remove structure induced by local sea ice cover (Figure 2a). These fields were obtained using the domain averages of 12 hourly fields from the interim reanalysis of the European Centre for Medium Range Weather Forecasts (ECMWF); [*Berrisford et al.*, 2011]. This approach allowed the orographic variability in wind fields to influence the model bulk computations [*Large and Pond*, 1981] of surface momentum and freshwater fluxes, while removing potential biases from surface temperature and humidity structure that would be inconsistent with the ice-free ocean model. To prevent excessive cooling in the exposed (ice-free) model ocean, no heat flux was applied through the ocean's surface. Surface freshwater fluxes were imposed as equivalent salt fluxes, consistent with the Boussinesq volume-conservation approximation to mass conservation.

The ocean model was initialized on 15 January 2005, and the modeled fields were spun up over 30 days of constant 15 January forcing followed by a year (the period 15 January 2005 to 31 December 2005) of time-dependent forcing. (HYCOM fields were unavailable for 1–14 January 2005.) The simulation was then continued through a second year of the same 2005 forcing and time-dependent boundary conditions. Model results from the initial spin-up month and year were discarded. All analyses were based only on results (6 hourly output files) from the second year, by which time the simulation had essentially reached statistical equilibrium with the open-boundary and surface conditions; for the analysis year, the annual mean, depth-averaged values of the local rate of change $\partial S/\partial t$ of salinity were of order $\pm 1\times 10^{-7}$ per day or smaller.

In addition to this simulation, denoted "ocean-only," a second simulation was conducted, denoted "ocean-ice," using the same spin-up and discard procedure, but with the ocean model coupled to a sea ice model.

The sea ice model [*Losch et al*., 2010] solved thermodynamic and dynamic equations for ice thickness, snow thickness, fractional ice area, and ice velocity, using ice horizontal-momentum equations solved following *Hunke and Dukowicz* [1997] and including direct ice-ocean stress with an ocean-ice interfacial drag coefficient $C_D \times \rho_w = 5.5$ (where ρ_w is the density of seawater), and zero-order thermodynamics allowing for snow cover [*Semtner*, 1976; *Hibler*, 1980; *Zhang et al*., 1998]. Ice concentration was prescribed at the open boundaries using data from the AMSR-E 12.5 km product (Figure 2c) [*Cavalieri et al*., 2014], with open-boundary ice thickness taken as 4 m and 1.5 m times the ice concentration fraction at the northern/western and southern/eastern boundaries, respectively. Sea ice model parameters were selected so that primarily landfast ice was established north of 77°N throughout the simulation year. In Nares Strait itself, the region of the domain with along-strait coordinates between 150 and 750 km, simulated ice speeds were less than 0.1 mm s^{-1} for 99.9% of the grid cells throughout the simulation year, and ice coverage exceeded 95% for 98.5% of modeled fields throughout the simulation year. Unlike the ocean-only simulation, the ocean-ice simulation was forced with atmospheric heat fluxes, including radiative fields taken from ECMWF. However, since the ocean was isolated from atmospheric heat fluxes by the sea ice cover, these heat fluxes had little effect on the ocean response, and the resulting ocean temperature and salinity fields in the ocean-ice simulation differed primarily for dynamical reasons (section 3.2.4). The same wind stress fields were applied to the ocean and ocean-ice simulations, but within Nares Strait this stress was taken up in the ocean-ice case by the landfast ice surface and thus not transmitted to the ocean.

The 2 year long simulations, ocean-only and ocean-ice, allow for a comparison between the modeled response to ice-free and landfast-ice conditions within the strait over a time period sufficient to yield reliable mean model values for configurations that are subject to the same imposed time-dependent ocean open boundary conditions. Although Nares Strait is rarely completely free of ice cover, much of the strait typically experiences an annual shift between mobile and landfast ice conditions [*Kwok*, 2005]. The ocean-only simulation is taken here as representative of mobile ice conditions: although the presence of mobile sea ice can itself alter the exchange of momentum between the atmosphere and ocean, the main effect is simply the dramatic contrast between wind forcing at the surface in the ocean-only case and the under-ice drag that replaces it in the ocean-ice case. The modeled mean velocity fields in the ocean-only simulation are found to reproduce the basic observed structure of velocity fields under mobile ice (section 3.1). Similarly, the ocean-ice simulation is taken as representative of landfast-ice conditions, and is likewise found to reproduce the basic observed velocity structure under landfast ice. The use of two simulations with identical ocean lateral boundary conditions allows systematic comparison and direct interpretation of the differences in model response with and without landfast ice, based on complete year-long simulations. Questions regarding the seasonality and spatial extent of landfast and mobile ice cover and the associated ocean response, including optimization of the ice model to represent most faithfully the observed seasonal cycle in Nares Strait, are deferred to future work.

Both simulations are strongly influenced by the HYCOM-derived boundary conditions imposed at the open lateral boundaries, the physical validity of which is uncertain given limited observational constraints and coarse resolution in this region of the HYCOM domain. Our interpretation of the model results, therefore, focuses on features that develop internally, within the domain, and on the dynamics that connect the internal circulation to the boundary conditions. For example, while the total volume transport through the channel is controlled by the imposed open-boundary conditions, surface forcing (wind stress or ice drag) and internal dynamics (e.g., instabilities, vertical mixing, and baroclinic adjustment) can alter important aspects of the circulation's structure within the strait. We rely on two basic approaches to achieve this separation of boundary-controlled and internally determined responses. First, we evaluate and compare the annual-mean properties of the ocean-only and ocean-ice simulations, which differ only in surface boundary condition. Second, we evaluate independently for each simulation the temporal variability and its connection to the boundary forcing using an empirical orthogonal function analysis. In general, we are less concerned with a precise match of modeled and observed fields, and more concerned with the representation of key features of the circulation, particularly with regard to the distinction between mobile versus landfast ice conditions.

3. Observed and Modeled Fields

3.1. Mean Velocity Structure

The CATS measurements have shown that the seasonal-mean, along-channel current across southern Kennedy Channel shifts between two characteristic states depending on sea ice conditions [*Rabe et al*., 2012].

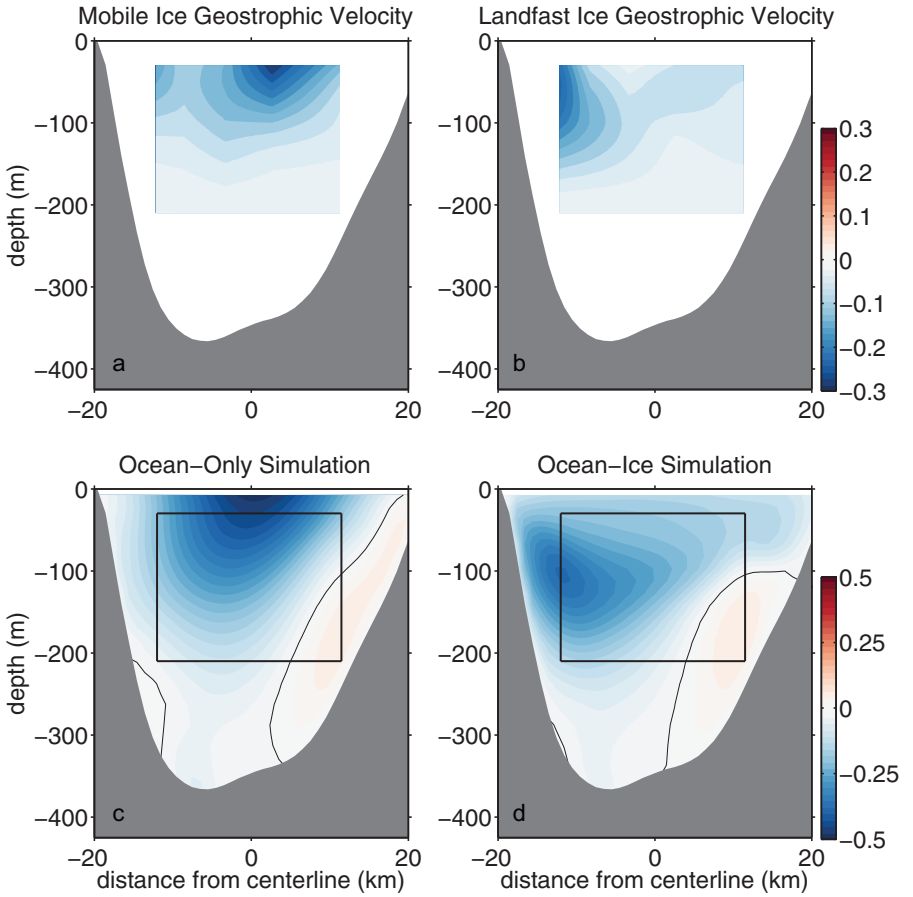

Figure 3. Geostrophic velocity reproduced from *Rabe et al*. [2012] for periods of (a) mobile and (b) fast ice conditions. Annual mean along-strait velocity from (c) the ocean-only simulation and (d) the ocean-ice simulation. (bottom) The zero-velocity contour (black). Note that different color scales were used in Figures 3a, 3b and Figures 3c, 3d to highlight structural detail.

Under mobile ice (including any ice-free conditions), a surface-intensified jet is located near the centerline of the strait (Figure 3a). Under landfast ice, a subsurface jet is offset to the western side of the strait (Figure 3b). *Rabe et al*. [2012] estimated that this alteration in current structure was accompanied by an increase of 20% in equivalent freshwater transport during mobile-ice conditions relative to landfast-ice conditions. These seasonal mean currents, which were calculated based on a geostrophic balance with the measured mean density field and a reference velocity from 200 m depth, are robust and well estimated from the multiyear observational data set [*Rabe et al*., 2012], even though the subtidal variability can reach 30–50% of the mean flow at a given time [*Münchow and Melling*, 2008].

Collectively, the ocean-only and ocean-ice simulations reproduce this basic, structural response to ice conditions. The ocean-only simulation has a surface-intensified jet located near the centerline of the strait (Figure 3c), similar to the observed structure under mobile-ice conditions. The ocean-ice simulation has a subsurface jet located on the western side of the strait (Figure 3d), similar to the observed structure under landfast ice. Both the across-strait positions and vertical distribution of the modeled annual-mean currents agree well with the respective observed mean currents from mobile-ice and landfast-ice periods (Figures 3c and 3d). The simulations generally have stronger southward velocities than the observed geostrophic estimates, however, this difference can be partly reconciled by adjusting the modeled fields to match the reference velocity used by *Rabe et al*. [2012].

Another characteristic feature of the observed circulation is a region of northward flow along the eastern side of Kennedy Channel under both mobile-ice and landfast-ice conditions. The northward flow is apparent in the directly measured long-term mean velocity fields [*Münchow and Melling*, 2008], which offer higher resolution than the geostrophic estimates of *Rabe et al*. [2012]. Annual-mean velocity sections from both

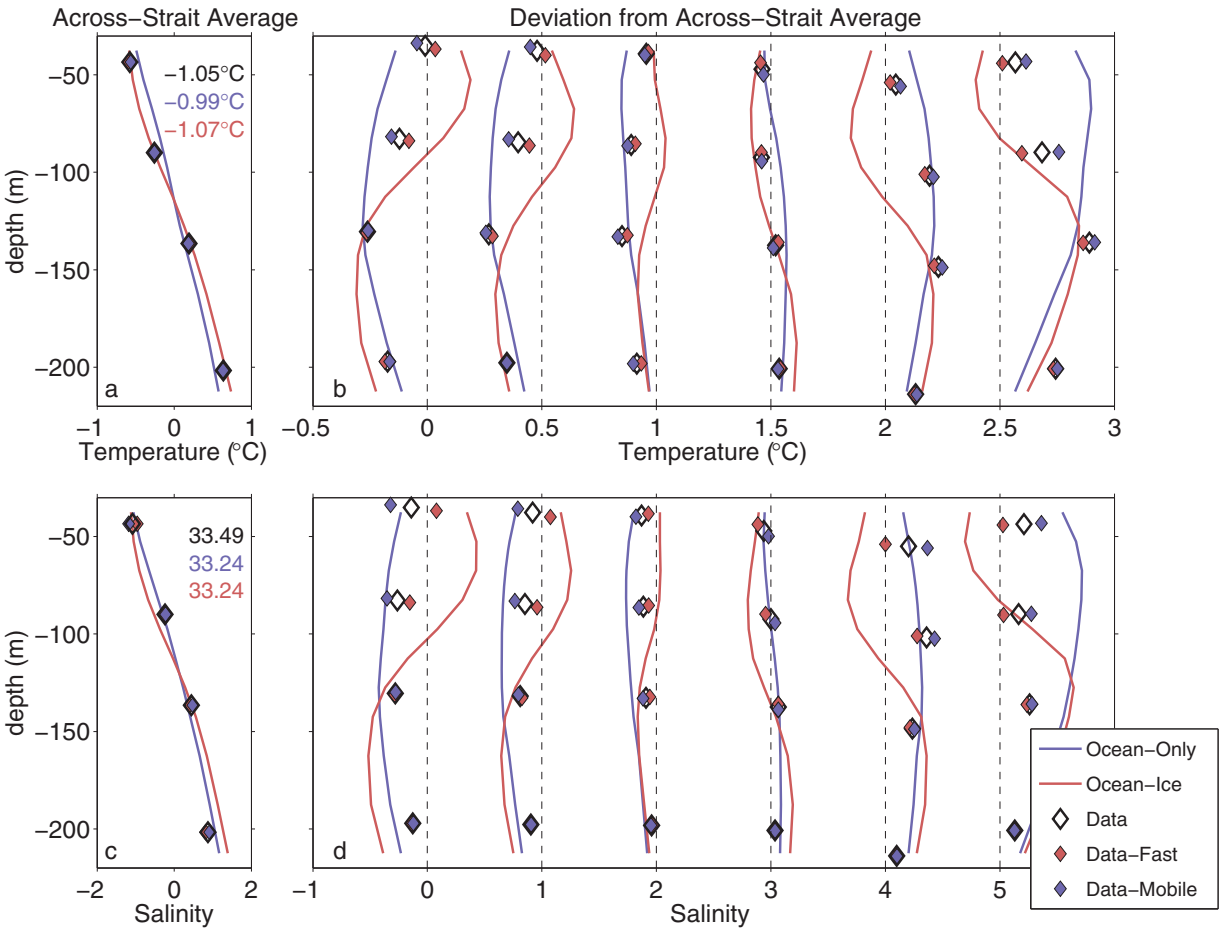

Figure 4. Comparison of (a, b) temperature and (c, d) salinity between the models (lines; ocean-only in blue and ocean-ice in red) and CATS observations (markers; annual mean in black, mobile-ice mean in blue, and landfast-ice mean in red). Across-strait average profiles (Figures 4a, 4c) are referenced to the mean values of temperature and salinity given in black (observations), blue (ocean-only), and red (ocean-ice). Deviations from the across-strait mean (Figures 4b, 4d) are successively offset by 0.5°C and 1 salinity unit moving eastward. Offsets in both plots are indicated by the dashed vertical lines. Model cells closest to the mooring locations are used for comparison. The landfast ice season was estimated as 1 January to 15 June 2005, and the mobile ice season was estimated as 16 June to 31 December 2005. For observational details, see *Rabe et al*. [2010].

the ocean-only and ocean-ice simulations show a qualitatively similar northward flow along the eastern side of the strait (Figures 3c and 3d).

The agreement between the modeled and observed response to changes in ice cover is a fundamental result of this study and is consistent with the hypothesis that the observed shift is a local response to sea ice conditions in the strait. We return to a more detailed examination of mean and fluctuating components of the modeled circulation throughout the strait after first comparing the modeled and observed statistics.

3.2. Comparison to Mooring Data

Model temperature and salinity were compared with CATS observations using grid cells closest to moored sensor locations (24 model cells based on the 4 by 6 moored array). The corresponding annual and cross-sectional mean temperatures are (−0.99, −1.07, −1.05) ° C for the ocean-only, ocean-ice, and observations, respectively. The annual and cross-sectional mean salinity in the simulations (33.24 for both cases) is low compared to the observed 33.49. The modeled, cross-sectional mean profiles of temperature agree to within 0.2°C of the observed value (Figure 4a). Above 125 m depth, the ocean-only simulation tended to be slightly warm on the eastern side of the strait and cool on the western side, while this pattern was reversed in the ocean-ice simulation (Figure 4b). The cross-sectional mean salinity was within 0.15 of the observed value at all depths for the ocean-only simulation and within 0.4 of the observed value in the ocean-ice simulation (Figure 4c). As with temperature, the salinity biases differed depending on across-strait position (Figure 4d). Above 125 m, the ocean-only simulation was too salty in the east and too fresh in the west. Biases in the ocean-ice simulation

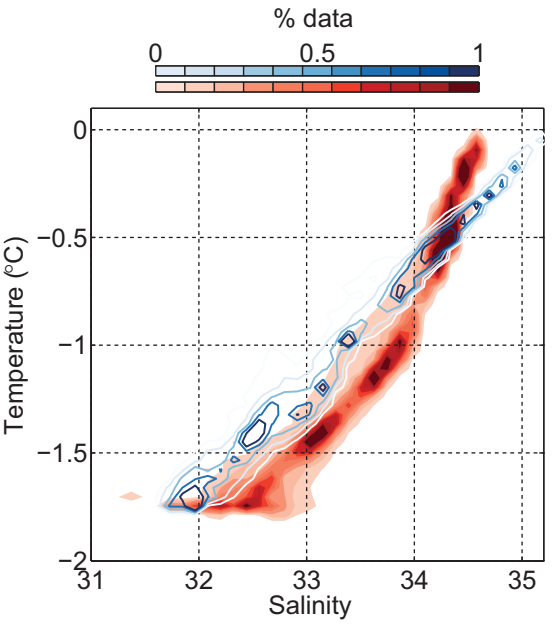

Figure 5. Temperature-salinity plot for the combined ocean-only and ocean-ice simulations (blue contours) and the CATS data (red-shaded contours). Model histograms are composed of 6 h data from cells closest to mooring sensors.

were generally greater and of the opposite sign. In both simulations, the biases in temperature and salinity tended to decrease with depth (Figures 4b and 4d). Comparisons based on separate consideration of mobile and landfast-ice periods modestly improve the agreement between observed and modeled fields.

The modeled temperature and salinity deviations from the across-strait means are strikingly similar to one another (compare Figures 4b and 4d). This tendency reflects a near-linear temperature-salinity (TS) relationship in the simulations (Figure 5). A combined TS distribution for the simulations is presented since individual distributions are nearly identical. The general orientation in TS space of the modeled TS distribution differs from the observed; however, the two distributions overlap within the deep warm, salty water (roughly $T = -0.5°C$ and $S = 34.2$). For temperatures less than $-0.5°C$, modeled salinities are generally fresher than observed, while for temperatures greater than $-0.5°C$, modeled salinities are generally more saline than observed. The overall mean temperature, mean salinity, and the across-strait average deviations in temperature and salinity (Figures 4a and 4c) agree reasonably well with the observed values. This agreement is largely a reflection of the bias-corrected fields prescribed at the open ocean boundaries. In contrast, the cross-strait differences in the structure of temperature and salinity profiles between the two runs primarily reflect changes in current structure rather than modification of TS properties.

The distribution of observed subtidal velocities (12 h averages) are compared to the modeled distributions using data from an acoustic Doppler profiler moored near the 300 m isobath offshore of Ellesmere Island and modeled fields spanning three across-strait cells (≈2 km) nearest the mooring location (Figure 6a). Model depths outside the range of the measured velocity were excluded in the comparison. The

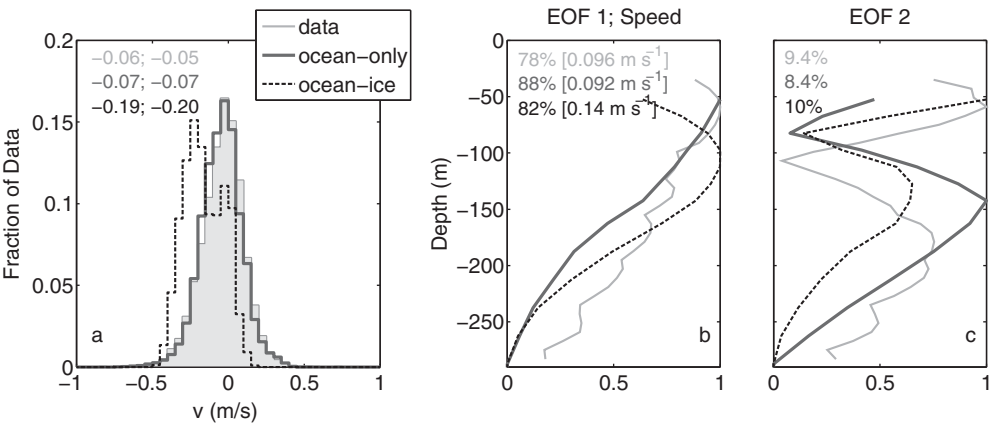

Figure 6. (a) Histograms of the along-strait velocity from a CATS acoustic Doppler profiler (light gray, shaded), the ocean-only simulation (thick dark gray), and the ocean-ice simulation (thin-dashed black). (top, left) Mean and median values. (b-c) Leading two EOFs of the modeled and measured speed. (top) The captured variance is shown in left-hand corner of each plot. The standard deviation is given in Figure 6b. CATS data were averaged into 12 h bins for comparison to model output.

ocean-only simulation approximately reproduced the observed distribution, with a mean of -0.07 m s^{-1}, close to the observed -0.06 m s^{-1}. The ocean-ice simulation showed instead a multipeaked distribution with one peak centered near zero (as with the data) and a second near -0.25 m s^{-1}, giving mean and median values that were biased negative, relative to measurements. The standard deviations of the model velocity distributions were 0.09 and 0.14 m s^{-1} for the ocean-only and ocean-ice simulations, respectively, within 10% and 50% of the observed value of 0.096 m s^{-1}.

The leading two empirical orthogonal functions (EOFs) of the observed and modeled velocity profiles are similar in structure and variance contribution (Figure 6b). The first mode captures 78, 88, and 82% of the variance in the data, ocean-only simulation, and ocean-ice simulation, respectively. The modeled current speed falls off more rapidly in depth than the observed current. The vertical location of the reversal in the second mode is reproduced to within 25 m by the model (Figure 6c); this offset is comparable to the model grid spacing of 15 m at this depth.

In addition to approximately reproducing these observed temperature, salinity, and velocity statistics at the CATS mooring line, the simulations also systematically developed a cyclonic eddy structure at the entrance to Petermann Fjord, similar to a feature that has previously been observed [*Johnson et al*., 2011]. This eddy, which is strongest in the ocean-only simulation, apparently develops from instability processes that also support a larger amplitude of temporal variability in the ocean-only simulation relative to the ocean-ice simulation (section 5).

4. Modeled Annual Mean Circulation

4.1 Velocity

The annual-mean volume transport -1.16 ± 0.46 Sv (annual mean $\pm$ one standard deviation) is the same for both simulations since it is set by the northern and western inflow boundary conditions. The cross-sectional structure of the along-channel flow can be, and is, different in the two simulations (Figure 7). The southward depth-integrated flow between Robeson and Kennedy Channel is located midstrait in the ocean-only simulation (Figure 8a). In contrast, the southward flow is concentrated along the western boundary in the ocean-ice simulation (Figure 8b). Both simulations show weak northward flow, typically located at depth along the eastern boundary, over much of the domain. However, even when computed as the integral over only northward annual-mean velocities, this northward transport does not extend uniformly or even continuously to the northern boundary (Figure 8d). At Smith Sound, for example, this northward transport is 0.3 and 0.1 Sv in the ocean-only and ice-ocean simulations, respectively, relative to 0.5 Sv at the interior edge of the northern boundary sponge region.

At the Robeson Channel cross-section, the annual mean flow is characterized by two southward jets, one along the western side of the strait and the other along the eastern side of the strait in both the ocean-only and ocean-ice simulations (Figures 7a and 7f). In both simulations, the western jet has a maximum southward velocity subsurface at roughly 125 m depth. The eastern jet is surface-intensified within the ocean-only simulation, but has a subsurface core in the ocean-ice simulation, located at roughly the same depth as the western jet. These two jets are distinguishable for roughly 40 km farther to the south in the ocean-only simulation and 50 km in the ocean-ice simulation. The southward flow eventually shifts into a single jet configuration within Kennedy Channel (Figures 7c and 7h).

Within Kennedy Channel, the model response is dependent on the surface boundary conditions (Figures 7c, 7d, 7h, 7i). The ocean-only simulation has a surface intensified jet approximately centered over the deepest portion of the channel, while the southward flow in the ocean-ice simulation maintains a subsurface maximum at roughly 125 m depth with a core constrained against the western side of the strait. This difference in mean cross-sectional structure is consistent with the characteristic behavior apparent in the CATS observations during mobile and landfast-ice conditions (section 3.1). Farther to the south, both simulations develop a stronger northward flow along the eastern side of the strait, although the magnitude of the northward flow is greater in the ocean-only simulation. By the southern Kane Basin (Smith Sound) section, the difference between the two simulations is pronounced, as maximum values reach 0.27 and 0.06 m s^{-1} in the ocean-only and ocean-ice simulations, respectively.

A striking difference between the two simulations is that regions of recirculation in the ocean-only simulation, including the entrance to Petermann Fjord and several locations within Kane Basin, are greatly reduced

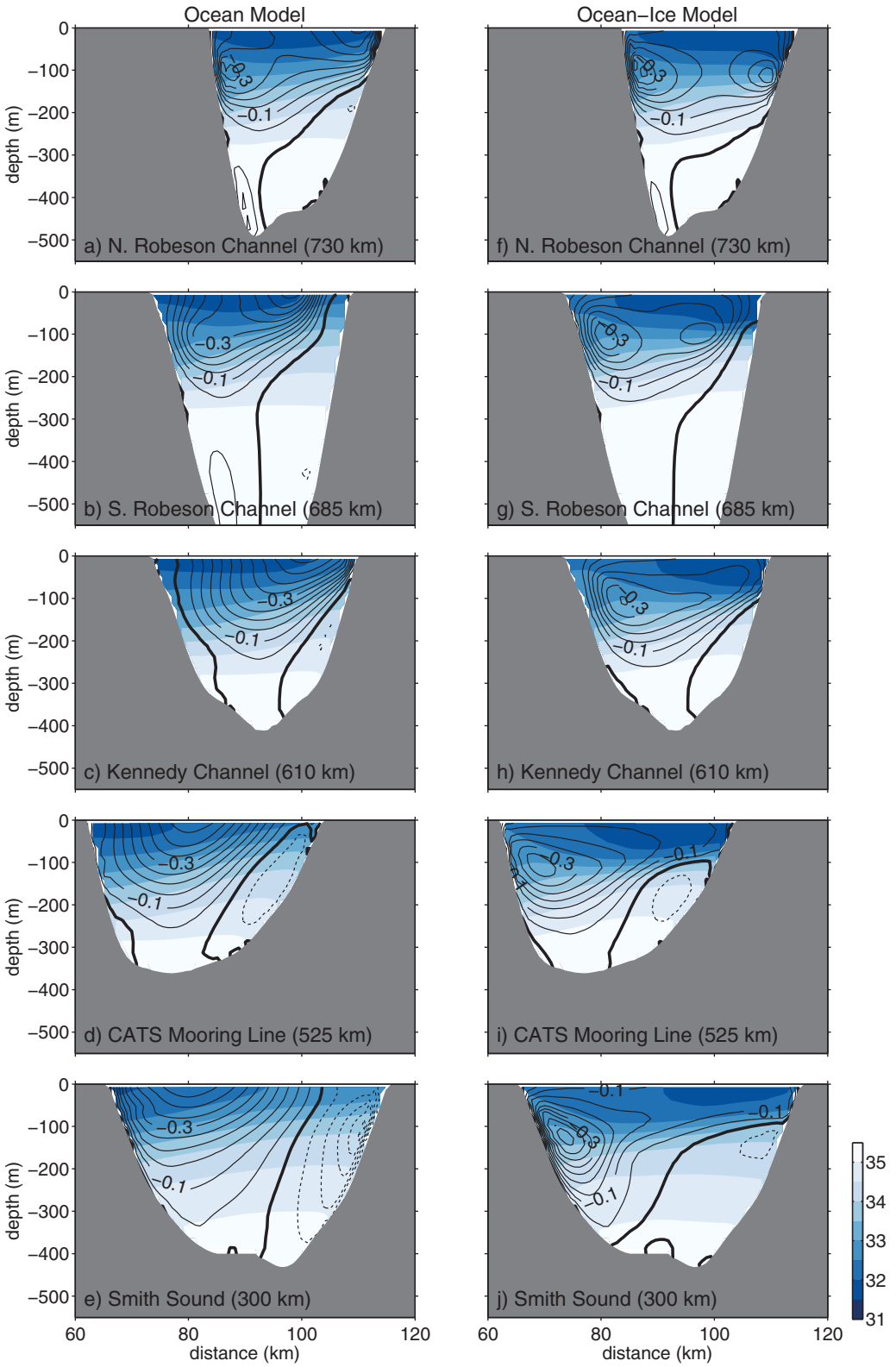

Figure 7. Annual mean salinity (shading) and along-channel velocity (contours) for the ocean-only (left) and ocean-ice (right) simulations across (a, f) northern Robeson Channel, (b, g) southern Robeson Channel, (c, h) Kennedy Channel, (d, i) the CATS mooring line, and (e, j) Smith Sound.

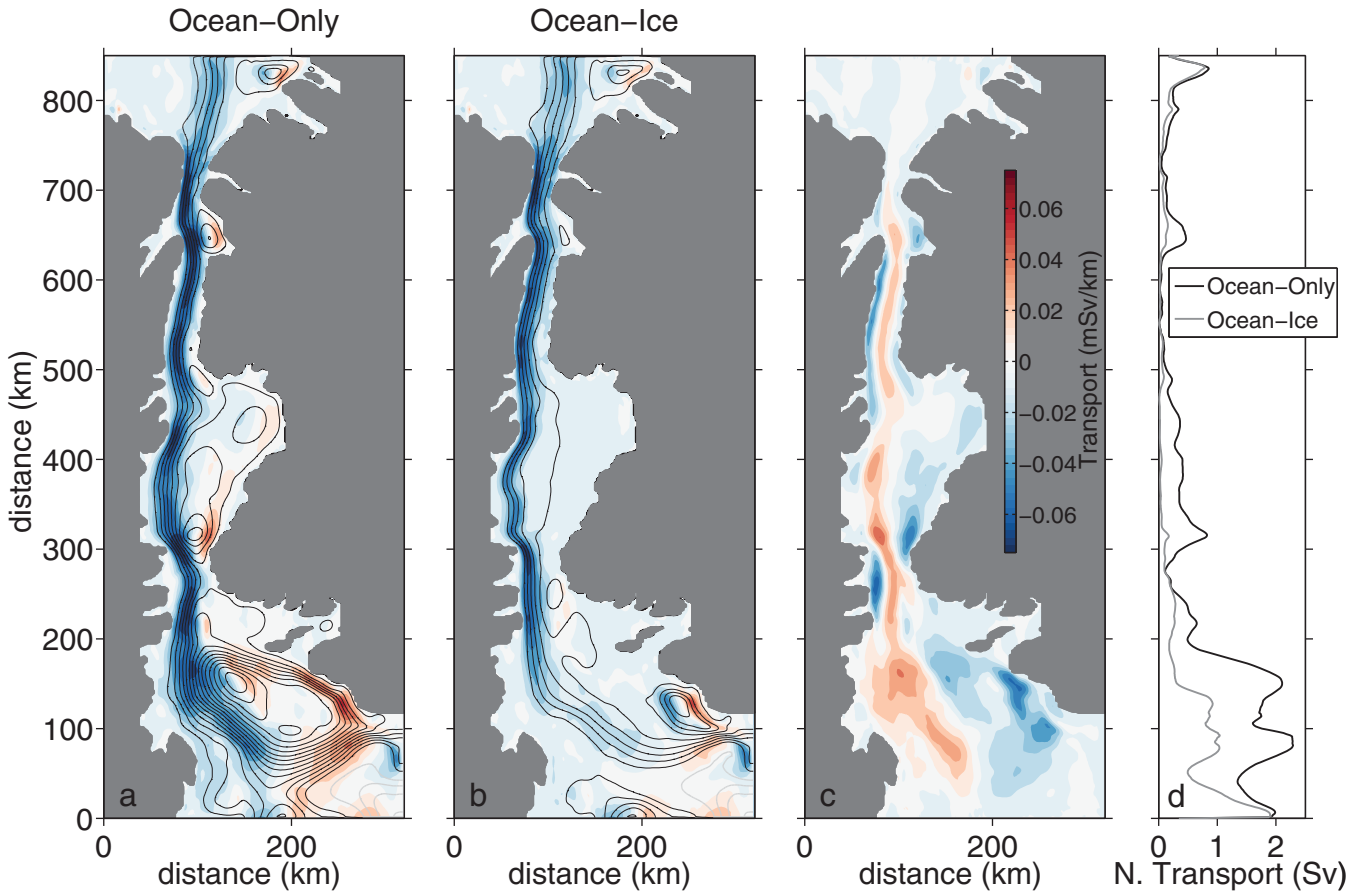

Figure 8. Annual mean barotropic streamlines (black contours) and the annual mean along-strait transport (shading) for the (a) ocean-only and (b) ocean-ice simulations. (c) Difference in transport between the ocean-ice and ocean-only simulations. (d) The northward transport—computed as the integral of all northward annual-mean velocities—for the ocean-only (black) and ocean-ice (gray) simulation.

or eliminated in the ocean-ice simulation (Figure 8). The recirculation at the mouth of Petermann Fjord is due to the intermittent appearance of a time-dependent eddy structure in the ocean-only case, a feature that also appears but is less energetic in the ocean-ice case. Perhaps notably, this region marks the transition between the double jet configuration characteristic of Robeson Channel and the single jet configuration in Kennedy Channel. Recirculations outside Nares Strait proper, near the northern and southern ends of the computational domain, are likely related to the imposed open boundary conditions.

4.2 Salinity

In general, salinities increase systematically towards the south in both simulations. The annual-mean, depth-averaged salinity between the surface and 150-m depth increases from 32.5 to 33 (32.4–32.7) between northern Robeson Channel and Smith Sound for the ocean-only (ocean-ice) simulation (Figure 9). The freshest waters typically reside along the western boundary in the ocean-only simulation, and mid-strait in the ocean-ice simulation. Despite this difference in mean structure, the annual-mean southward freshwater transports through the strait are similar—70 and 63 mSv for the ocean-only and ocean-ice simulations, respectively, referenced to salinity 34.8. Although these values are high compared to some estimates [*Münchow et al*., 2006], they are generally in agreement with more recent estimates that attempt to extrapolate the observed freshwater flux to the surface [*Münchow*, 2015].

In the annual means of both simulations, two dominant modes of volume transport by salinity class, a primary mode near $S = 32$ and the secondary mode near $S = 33$, are superimposed upon a more diffuse southward continuum. Only a few of the high-salinity classes ($S > 34.8$) have a weak net northward transport in the vicinity of Smith Sound. The along-strait transformation of the flux is detailed by the zonally integrated volume transport in three broad salinity classes defined by two intermediate salinity values $S = \{32, 34\}$

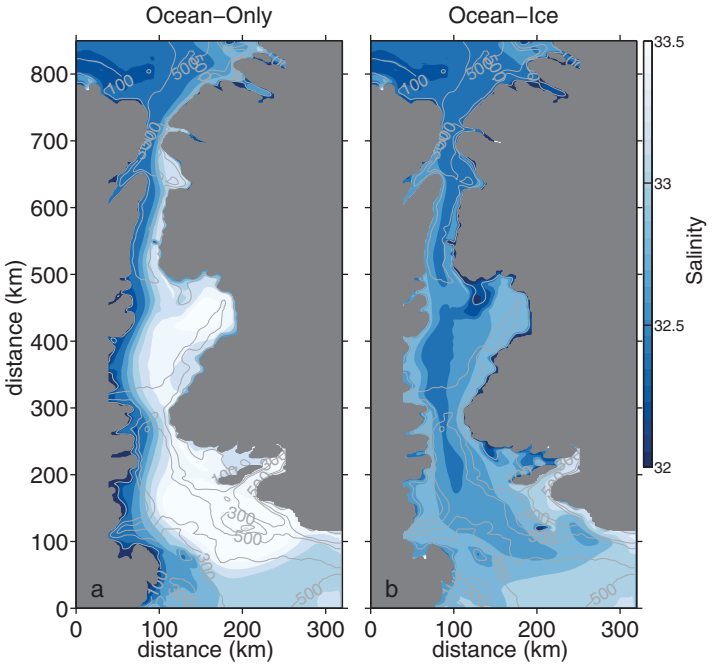

Figure 9. Annual mean salinity depth-averaged between 0 and 150 m for the (a) ocean-only and (b) ocean-ice simulation. The 100, 300, and 500 m isobaths are contoured in gray.

(Figure 10). For this calculation, regions of open western or eastern boundary were closed along the boundary by calculating the meridional integral of the zonal transport by salinity class from the zonal cross section to the nearest closed boundary location. The total cross-sectional volume transport integrated over all classes is then equal to the total annual-mean transport of roughly 1.2 Sv southward at each meridional position.

The changes in volume transports with along-channel distance in these three classes are consistent with systematic exchanges between neighboring salinity classes by vertical mixing during southward transit through the channel. The southward decrease in southward volume transport in the freshest layer, $31 < S < 32$, is compensated by increasing southward volume transport in the layer $32 < S < 34$. Exchange across the 34 salinity surface is negligible. Consequently, the total southward volume transport for $S < 34$ is nearly constant in the channel at about 1 Sv, and volume transport for $S > 34$ is nearly constant at about 0.15 Sv. Transport in the fresher salinity classes ($S < 34$) are enhanced in the ocean-only simulation relative to the ocean-ice simulation; likewise, transport within the most saline class ($S > 34$) is enhanced in the ocean-ice simulation relative to the ocean-only simulation.

The cross-channel structure of meridional volume transport within specific salinity classes differs in the two cases. For the ocean-ice simulation, the freshest water ($S < 32$) is largely confined to the eastern side of the

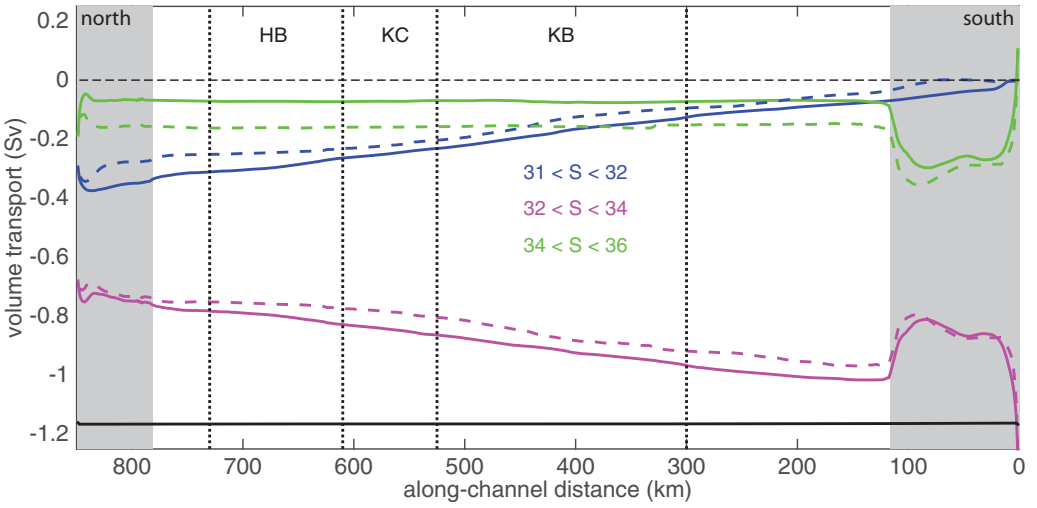

Figure 10. Zonally integrated meridional volume flux versus distance along channel in three salinity classes ((thick solid); $S < 32$ (blue), $32 < S < 34$ (magenta), and $S > 34$ (green)) for the ocean-only (solid lines) and ocean-ice (dashed lines) cases. Also shown is the total transport summed over all salinity classes (black). The locations of Kane Basin (KB), Kennedy Channel (KC), and Hall Basin (HB) are indicated by vertical dashed lines.

channel, while the remaining net transport (salinity classes $S > 32$), which is the bulk of the total transport, is largely confined to the western side of the channel (Figure 11de). For the ocean-only simulation, the net southward volume transport for all salinity classes is concentrated in the center of the strait (Figure 11ab); however, some intermediate salinity waters are also transported northward along the eastern side of the strait from the southern end of the strait to north of the mooring line. In both simulations, the net southward transport for classes with $S > 34$ is confined to salinity classes with salinity less than 34.8. The volume transport for classes with $S > 34.8$ is confined to separate recirculations north and south of Kane Basin, with northward flow on the eastern side of the channel and southward flow on the western side of the channel, and essentially zero net transport (Figure 11cf). The portion of Kane Basin separating these deep recirculations is shallow, with bottom depths less than 300 m.

The shift in velocity and salinity structure between the two simulations is accompanied by a change in the distribution of heat, which has little effect on density and thus on internal ocean dynamics, but can potentially affect ocean-ice interactions. Along the eastern side of the strait, temperatures above 100 m tend to be 0.5–1.0°C warmer in the ocean-only simulation than in the ocean-ice simulation. Temperatures at depth are a few tenths of a degree cooler in the ocean-only simulation than in the ocean-ice simulation. These differences are consistent with relatively cool surface waters being displaced to the east in the ocean-ice simulation.

5. Temporal Variability

5.1. Statistical Formulation

Because of the enclosed channel geometry, the imposed inflow through the northern and western open boundaries has a significant influence on the circulation even at distances well removed from the edges of the domain. For example, the integrated transport through any model cross section adjusts almost instantaneously to the transport entering through the open boundaries because the model fluid is incompressible in the standard Boussinesq sense. More generally, adjustment to variability imposed at the open boundaries can occur on a wide range of space and time scales. A combination of empirical orthogonal function (EOF) and lagged cross-correlation analysis is used here to distinguish modes of variability that are controlled by inflow at the upstream boundary from those that are driven by local forcing or may arise internally from instability processes.

EOFs (Figure 12) for salinity, $\phi_i^S(x,z)$, and velocity, $\phi_i^V(x,z)$, with corresponding temporal amplitudes $s_i(t)$ and $v_i(t)$, indexed by mode number i, were computed separately at Robeson Channel, the CATS mooring line, and Smith Sound cross-sections after removal of the point-wise annual mean values from the cross-sectional fields. The salinity and velocity EOFs were computed independently, and no geostrophic constraint was applied; however, a thermal wind balance, $\partial\phi_j^S/\partial x \approx \partial\phi_k^V/\partial z$, between the j-th salinity and k-th velocity EOFs does in some cases emerge, with corresponding amplitudes $s_j(t)$ and $v_k(t)$ that are strongly correlated ($R \gtrsim 0.75$) with each other.

The leading modes of variability were assessed by computing lagged cross correlations of the EOF amplitude time series with a subset of time series representing the upstream boundary conditions: the total volume transport, total freshwater transport, and temporal amplitudes of leading salinity EOFs at the northern boundary. The local forcing was assessed using the cross correlation of EOF amplitudes with a measure of the local average of the wind stress. For this analysis, winds were averaged between Robeson Channel and the mooring line, and then filtered using a running weighted average with weight increasing linearly from zero at time t – 10 days to a maximum at time t. Since the wind stress has previously been shown to be highly correlated within Nares Strait [*Samelson and Barbour*, 2008], the same wind metric is used for each cross section. Using these methods, some EOFs can be attributed primarily either to boundary influence, local surface forcing, or internal variability. However, all EOFs likely contain some variance from all three sources, since the EOF procedure determines statistical and not dynamical modes. The discussion is therefore restricted to the leading EOFs with large variances and high correlations with the boundary inflow or local wind stress. All quoted correlations are significant at the 95% level with p values of 0.001 and smaller.

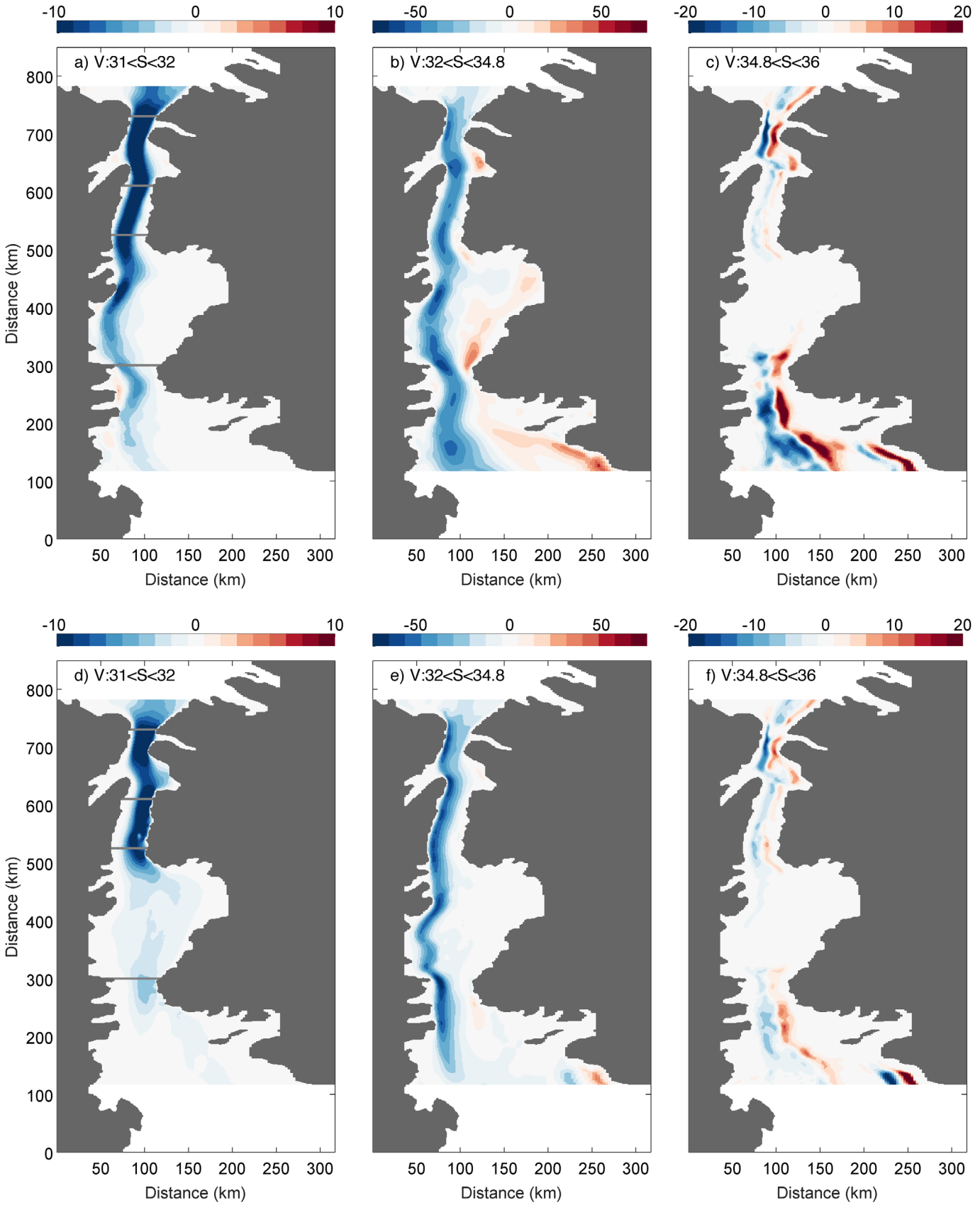

Figure 11. Meridional volume flux (10^3 m^2 s^{-1}) versus x and y in the zonally closed channel region in three salinity classes (a, d) $S < 32$, (b, e) $32 < S < 34.8$, (c, f) $S > 34.8$ for the (Figures 11a–11c) ocean-only and (Figures 11d–11f) ocean-ice cases. The cross-channel transects (gray) shown in Figures 11a and 11d enclose the Kane Basin, Kennedy Channel, and Hall Basin regions, as indicated in Figure 10.

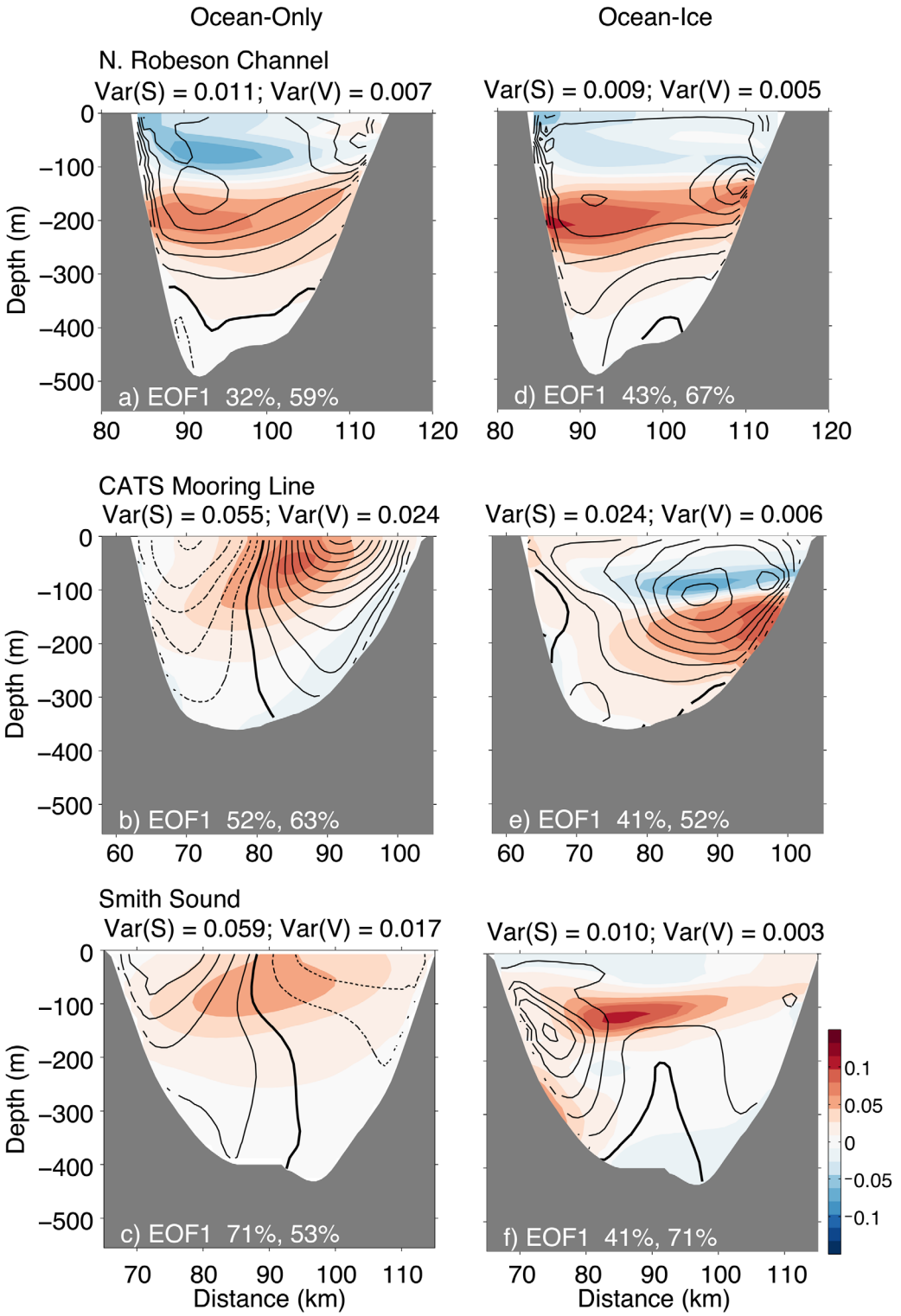

Figure 12. The first EOFs of salinity (shading) and velocity (black contours) across (a, d) Robeson Channel, (b, e) the CATS mooring line, and (c, f) Smith Sound for the ocean-only simulation (left plots) and the ocean-ice simulation (right plots). The total variance and explained variance (salinity, velocity) for each mode are given. The velocity EOF is plotted in increments of 0.01 (negative values-dashed contours, positive values-solid contours). The zero contour is shown in bold. EOFs are normalized so that $||\phi_i^*|| = \sqrt{\sum_j (\phi_i^*(x_j))^2} = 1$.

Table 1. Correlation Coefficients and Associated *p* Values Between the Listed Principal Components of Along-Strait Velocity and the Time Series of Volume Transport at the Northern Boundary for the Ocean Simulation and the Ocean-Ice Simulation

	Robeson Channel	Mooring Line	Smith Sound
Ocean-Only Simulation			
v_1	0.96 ($p = 0.000$)	0.48 ($p = 0.000$)	0.24 ($p = 0.000$)
v_2	−0.16 ($p = 0.000$)	−0.57 ($p = 0.000$)	−0.01 ($p = 0.717$)
v_3	−0.08 ($p = 0.002$)	−0.62 ($p = 0.000$)	−0.90 ($p = 0.000$)
Ocean-Ice Simulation			
v_1	0.98 ($p = 0.000$)	0.91 ($p = 0.000$)	0.96 ($p = 0.000$)
v_2	−0.12 ($p = 0.000$)	−0.37 ($p = 0.000$)	−0.18 ($p = 0.000$)
v_3	−0.07 ($p = 0.013$)	−0.12 ($p = 0.000$)	−0.06 ($p = 0.023$)

5.2. Response to Northern Inflow

Across northern Robeson Channel, a majority of the variability in the velocity field is related to the imposed inflow at the northern boundary. The leading-mode amplitude v_1 is strongly correlated with transport through the northern boundary for both simulations (Table 1 and Figure 13b). The corresponding EOF, ϕ_1^V, shows a near uniform structure across the strait (Figure 12). This mode contains more than half the variance at this location (59% and 67% for the ocean-only and ocean-ice simulation, respectively). The leading EOFs for salinity are more difficult to interpret but also appear to be related to northern boundary variability. The leading-mode amplitudes s_1 are not significantly correlated with the northern inflow in either simulation ($R < 0.4$ for both volume and freshwater inflows), but are correlated with each other ($R = 0.73$, Figure 13a), suggesting an underlying deterministic control by the boundary conditions. Salinity structure along the boundary contributes to this control, as s_1 at Robeson Channel is correlated with the amplitude time series s_2 computed for the northern open-boundary section with correlation coefficients $R = 0.70$ and $R = 0.64$ for the ocean-only and ocean-ice simulations, respectively.

In the ocean-ice simulation, the influence of the inflow conditions extends south of Robeson Channel. At both the Kennedy Channel and Smith Sound sections, the dominant modes of temporal variability are consistently correlated with the northern inflow (Table 1 and Figure 13) and account for more than half of the velocity variance (Figure 12). The second EOF of velocity is also related to the northern inflow, but the peak correlation occurs at a time lag of roughly 1 week ($R = 0.61$ at Kennedy Channel and $R = 0.45$ at Smith

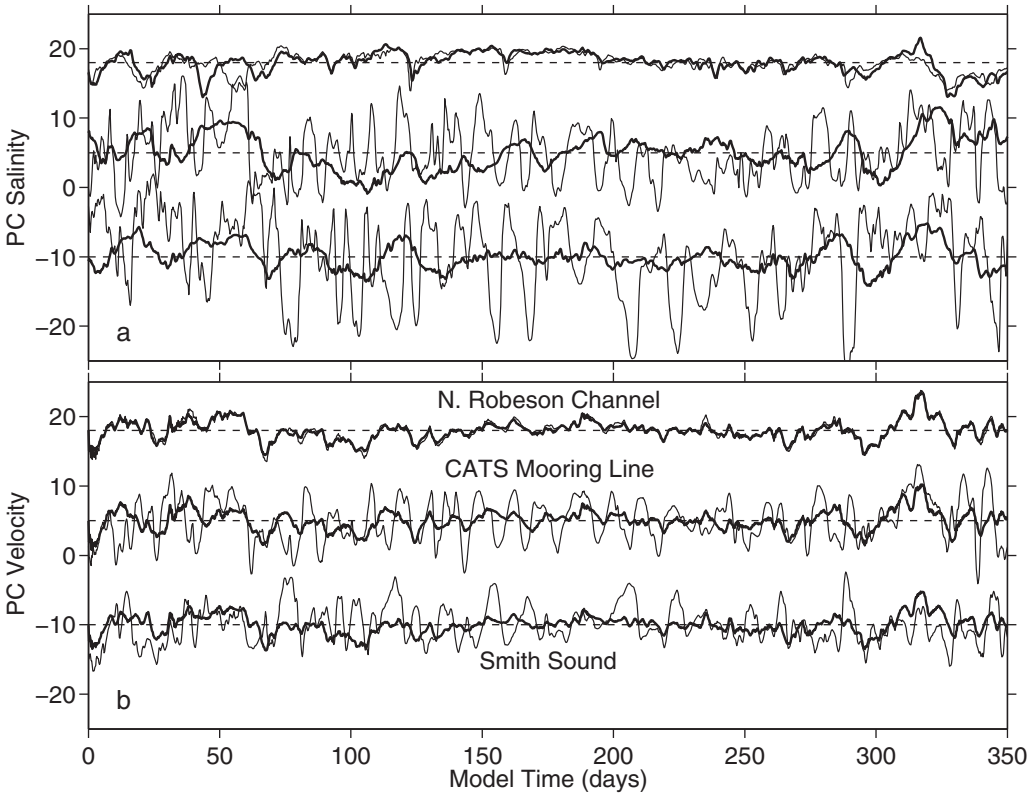

Figure 13. Amplitude time series of the ocean-only simulation (thin black) and ocean-ice simulation (thick black) for (a) salinity and (b) velocity (m s^{-1}) for the leading EOFs shown in Figure 12. Time series are offset by constants (thin-dashed horizontal lines at −10, 5, and 18) for visibility.

Sound). Collectively, these modes represent roughly 70–80% of the salinity and velocity variance in the ocean-ice simulation. At these sections, leading salinity and velocity modes are related ($R > 0.8$ in each case) through the thermal wind relation, and thus likely connected to the northern inflow as well. Note also that the leading-mode velocity amplitudes (v_1) are all similar to one another in the ocean-ice simulation (Figure 13), which further emphasizes their dependence on the inflow condition.

In contrast to the ice-ocean simulation, the percent of explained variance related to the northern inflow diminishes rapidly from north to south in the ocean-only simulation. The leading velocity mode is not strongly correlated with the northern boundary transport at either Kennedy Channel or Smith Sound (Table 1), and the corresponding amplitudes differ qualitatively from those of the ocean-ice simulation (Figure 13). At Kennedy Channel, the second and third velocity EOFs, which represent roughly 22% and 7% of the local variance, respectively, have slightly stronger correlation with the northern boundary inflow than the leading mode. At Smith Sound, the third EOF is most closely related to the boundary forcing ($R = 0.90$), and accounts for 14% of the total variance. Note that for the ocean-only simulation, the total velocity variance increases in the CATS and Smith Sound sections relative to that at Robeson Channel, so that the total variance attributed to northern boundary control decreases less than the attributed fractional variance. A similar set of conclusions holds for salinity in the ocean-only simulation (Figure 13).

5.3. Local Wind Forcing and Internal Variability

Unlike variability in the ocean-ice simulation, which is primarily controlled by the boundary conditions, variability in the ocean-only simulation arises primarily from internal dynamics and, to a lesser degree, from local wind-stress forcing within and southward of Kennedy Channel. At the CATS mooring section, the temporal amplitudes s_1 and v_1 of the leading ocean-only EOFs are correlated with $R = 0.84$ (Figure 13), but are not correlated with the inflow conditions at the northern boundary (Table 1). A similar pattern is observed in the leading EOFs at Smith Sound: $R = 0.86$ between s_1 and v_1, while each has low correlation with the northern boundary transport. The spatial EOFs at these locations are markedly different in the ocean-only and ocean-ice simulations (Figures 12b, 12e, 12c, and 12f). For the ocean-only simulation, v_1 corresponds to a weakening of the current on one side of the strait and strengthening on the other, rather than the near-uniform response observed at Robeson Channel and in all leading modes of the ocean-ice simulation. This asymmetric response is consistent with an east-west shift in the current, which at these sections is generally characterized by a single, surface intensified jet, as in the annual mean (Figures 7h and 7i).

South of Robeson Channel, the leading modes of salinity and velocity in the ocean-only simulation appear to be related to a fluctuating eddy feature that regularly develops in the vicinity of Hall Basin and Petermann Fjord, evidently through an internal, presumably baroclinic, instability. The period of the associated oscillation is roughly 12–15 days (Figure 13). These EOFs—and therefore, evidently, the instability—account for most of the salinity and velocity variance at the CATS mooring line (52% and 63%, respectively) and at Smith Sound (71% and 53%, respectively). An instability also develops in the ocean-ice simulation, but it is less energetic and less frequent; its signature does not appear clearly in any of the leading three EOFs of the ocean-ice simulation.

Salinity fields at the two southern sections in the ocean-only simulation are also influenced by wind forcing. At the CATS mooring line, the second EOF in salinity, which contains 24% of the variance, is lag-correlated with the ramp-weighted wind forcing, with correlation coefficient $R = 0.54$ at a lag of 12 h for s_2. Across Smith Sound, the second EOF in salinity, which contains 18% of the variance, is also correlated with the wind, with $R = 0.43$ at a 12 h lag for s_2. The across-strait structure of these two EOFs corresponds to freshening at depth and salinification near the surface when winds are southward. This signal is generally consistent with downwelling of fresher water on the western side and upwelling of saltier water to the east for southward wind-stress perturbations, and the opposite for northward perturbations.

6. Dynamics

Annual-mean horizontal momentum balances were computed from 10 day average momentum-balance terms saved as diagnostics from the numerical simulations. Upper-ocean balances were obtained by further averaging these annual-mean balances from the surface to 45 m depth (Figures 14 and 15). For both simulations, both horizontal components of the annual-mean momentum balance were primarily geostrophic, with the Coriolis force and pressure gradient terms typically 5–10 times larger than other contributions

(Figures 14a, 14e, 15a, and 15e). The different spatial structures of the across-strait pressure gradient and Coriolis force in the two cases reflect the shift in the mean circulation between the ocean-only and ocean-ice simulations. The ocean-only simulation is characterized by a surface-intensified jet; the signature of the jet is readily apparent in the momentum balance, with dominant geostrophic terms largest midstrait (Figure 14e). In contrast, the ocean-ice simulation exhibits a weaker across-strait pressure gradient and Coriolis force that is less structured (Figure 15e). Although a general offset towards the west is noticeable, this signal is more pronounced deeper in the water column (not shown), consistent with the subsurface intensification of the ocean-ice model jet.

The ageostrophic balances differ in the two cases. In the ocean-only simulation, the difference of along-channel pressure gradient and Coriolis force (Figure 14b) is balanced by a combination of nonlinear advection and southward surface wind stress (Figures 14c and 14d). The difference of the across-channel pressure gradient and Coriolis force (Figure 14f) is balanced almost completely by advection related to the eddy variability (Figure 14g). In contrast, in the ocean-ice simulation the former is balanced by the northwestward surface stress from ice drag that opposes the surface current (Figures 15d and 15h), while nonlinear advective terms are relatively weak. The stress in the ocean-ice simulation depends on the strength of the current, rather than the imposed wind forcing as in the ocean-only simulation. Coincidentally, the surface stress in the two simulations has roughly the same magnitude, but is of course oppositely directed (Figures 14d and 15d).

6.1. Ekman-Adjustment Model

The main differences in upper ocean response between the two simulations are consistent with the replacement of surface wind stress by surface drag from landfast ice, which should decrease the magnitude of the near-surface southward velocity and also induce an eastward surface Ekman transport proportional to the ice drag. The eastward surface Ekman transport should cause an eastward shift of the relatively fresh, near-surface isohalines, and perhaps also a westward shift in the geostrophically balanced current. Transport patterns (Figure 8) and salinity fields (Figure 9b) reflect this transition. Consequently, the transport of the freshest water borders the eastern coast in the ocean-ice simulation (Figure 11d), while intermediate salinity values are transported along the western side of the strait (Figure 11e). In contrast, transport of these salinity classes is roughly midstrait in the ocean-only simulation (Figures 11a and 11b).

The basic effect of the induced Ekman-layer flow associated with southward winds (ocean-only simulation) or landfast ice (ocean-ice simulation) can be illustrated with a steady, two-dimensional (cross-channel versus depth), linear model. This semianalytical model determines the modification of an inviscid, geostrophic along-channel flow by turbulent Ekman dynamics combined with appropriate boundary conditions in a rectangular channel. The complete model equations are provided in Appendix A, and only a brief description is given here.

The flow is decomposed into the basic inviscid, geostrophic component plus a disturbance that is induced by the turbulent Ekman diffusivities and the boundary conditions. Two cases are considered. The first is representative of the ocean-only simulation, with the turbulent stress at the upper surface matching the imposed wind stress. The second is representative of the ocean-ice simulation, with a no-slip (zero velocity) condition on the horizontal velocity at the upper surface. The remaining top, bottom, and side-wall conditions are the same for both cases. Vertical motions in the model are created by the convergence and divergence of the horizontal Ekman velocity. The basic geostrophic flow is chosen to have a level of no motion at the bottom of the channel, and an along-channel pressure gradient is allowed so that the flow can be maintained in the presence of ice and bottom friction.

This simplified model provides a quantitative and dynamically motivated illustration of the Ekman response to southward wind forcing and landfast ice. The solutions depend on the imposed pressure gradient as well as the surface boundary conditions. The pressure gradient is constrained by requiring the total volume transport in the simplified model to approximately match that imposed in the numerical simulations (1.2 Sv). The Ekman-adjustment model replicates several of the primary features observed in the two numerical simulations and, in doing so, strengthens the interpretation that the shift in current structure under landfast ice can be understood as a frictional response to the altered surface boundary condition on stress or horizontal velocity. In response to southward winds, the Ekman adjustment of the density field constrains the freshest water to the western side of the channel, intensifying the across-strait density gradient and enhancing the along-strait southward flow (Figures 16a, 16c, and 16e). Under landfast ice, the Ekman response

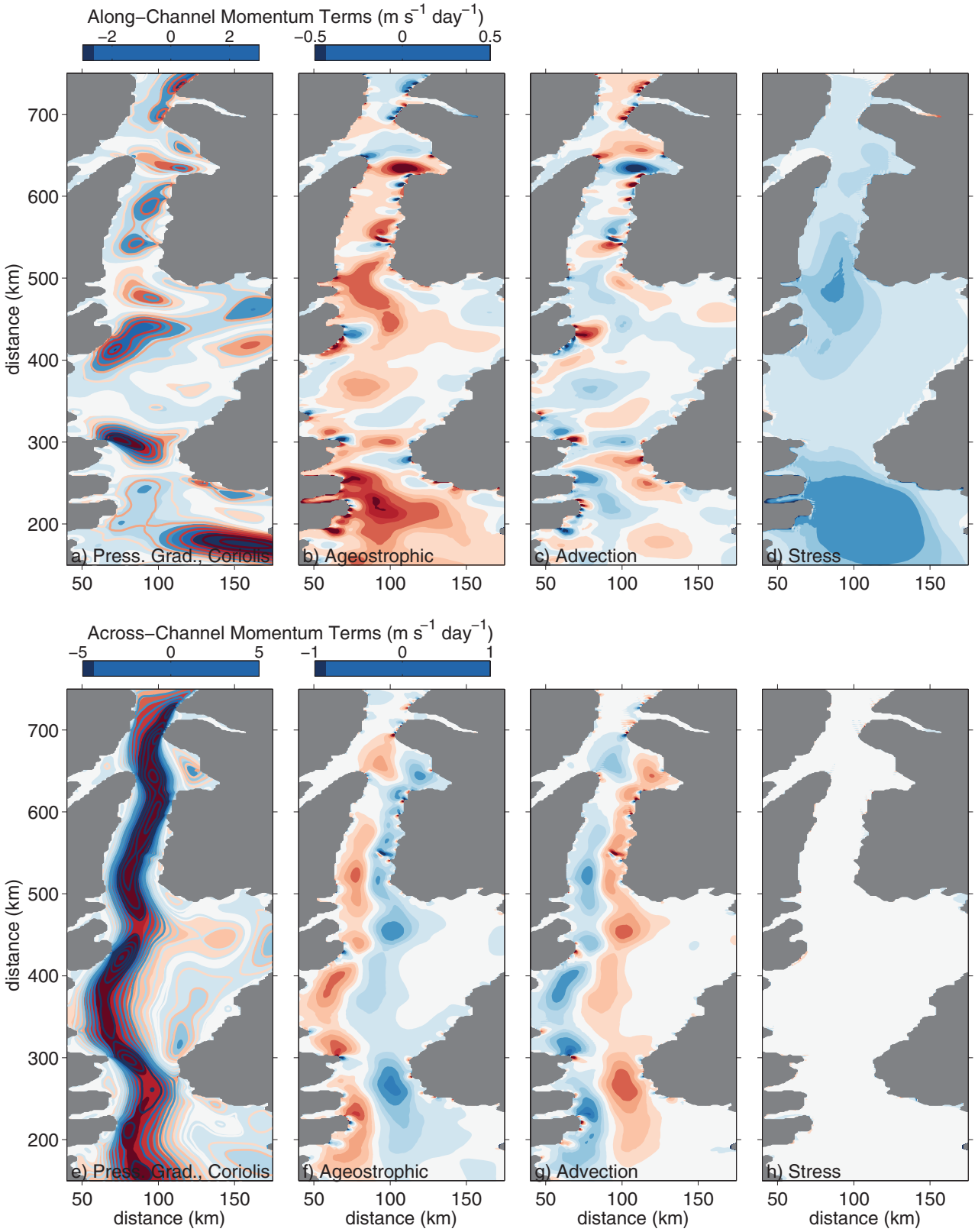

Figure 14. Annual mean contributions to the (a–d) along- and (e–h) across-channel momentum balances averaged over the upper 45 m for the ocean-only simulation. Figures 14a and 14e pressure gradient (shading) and Coriolis acceleration (contours), Figures 14b and 14f) ageostrophic contribution (sum of pressure gradient and Coriolis term), Figures 14c, 14g nonlinear advection, and Figures 14d, 14h stress. Note that the color scale in Figures 14a–14d differ from those in Figures 14e–14h. The sign of individual contributions reflects the corresponding influence to the tendency, i.e., all shown terms appear on the right-hand side of the momentum balance.

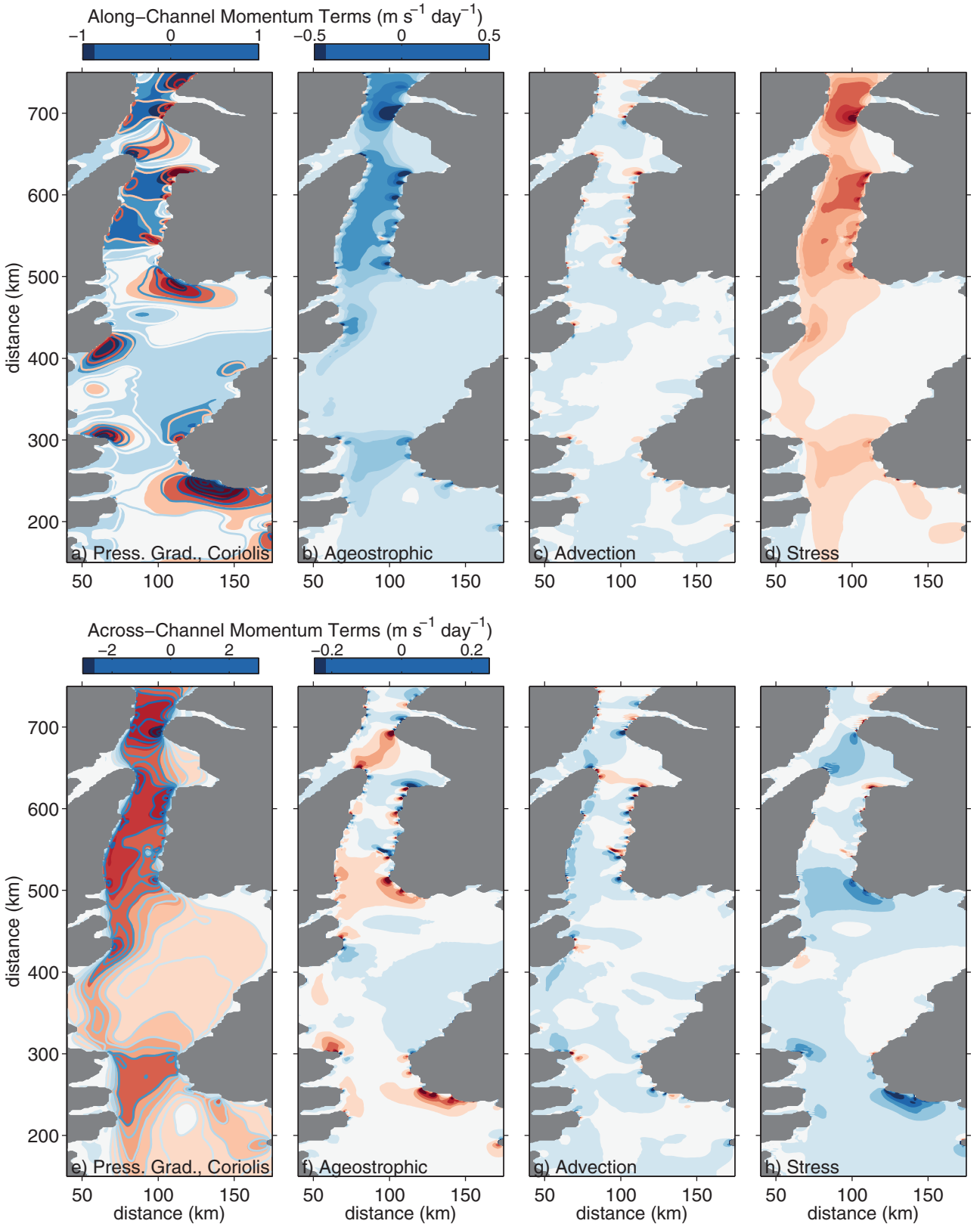

Figure 15. Annual mean contributions to the (a–d) along and (e–h) across-channel momentum balances averaged over the upper 45 m for the ocean-ice simulation. Figures 15a, 15e pressure gradient (shading) and Coriolis acceleration (contours), Figures 15b, 15f ageostrophic contribution (sum of pressure gradient and Coriolis term), Figures 15c, 15g nonlinear advection, and Figures 15d, 15h stress. Note that the color scale in Figures 14a–15d differ from those in Figures 15e–15h. The sign of individual contributions reflects the corresponding influence to the tendency, i.e., all shown terms appear on the right-hand side of the momentum balance.

modifies the upper ocean structure so that the near-surface density gradient is reversed, with the freshest water shifted toward the eastern side of the channel, and the along-channel flow has a subsurface core, located well below the upper boundary layer (Figures 16b, 16d, and 16f). These two basic features observed and modeled within Kennedy Channel, corresponding to the ocean-only simulation (observed mobile-ice conditions) and the ocean-ice simulation (observed landfast-ice conditions), respectively, are reproduced by this simple model (e.g., compare Figures 16c, 16d–16g, 16h and 7d, 7i).

In contrast, the linear Ekman-adjustment model does not and cannot reproduce the westward shift of the subsurface jet under landfast ice, because of symmetry properties following from the linearization of the model. However, a westward shift under landfast ice conditions would be qualitatively consistent with the general westward advection implied by the sign of the interior across-channel velocity (Figure 16f), so that the qualitative indication from the Ekman-adjustment model can be viewed as consistent with the observed shift. We also note that the along-stream evolution between Robeson and Kennedy Channel (Figures 7a, 7d and 7f, 7i) cannot be reproduced with this two-dimensional model. The westward shift of the current in Kennedy Channel, accordingly, may also reflect a preference in the ocean-ice simulation to favor development of the western jet downstream of Robeson Channel, whereas the ocean-only simulation favors the eastern jet.

7. Conclusions

The along-strait evolution of the currents and hydrography in Nares Strait have been examined using two simplified ocean simulations, one with an effectively landfast ice cover and the other ice free. These models reproduce the characteristic mean flow structures observed in Kennedy Channel during landfast and mobile-ice conditions, as well as basic aspects of the observed statistics of the time-dependent flow. The simulations, supplemented by a semianalytical local Ekman model, provide a dynamical rationalization of the observed shift in current structure between landfast and mobile ice conditions [*Rabe et al*., 2012]. The dynamical response to the surface frictional layer associated with either southward winds in the ocean-only simulation and landfast sea ice in the ocean-ice simulation not only results in a systematic change in the mean current structure that strongly controls the spatial distribution of heat and salt within the model domain, but also determines the primary modes of temporal variability within the domain. Furthermore, analysis of model results over the full length of the strait provide the regional context for the CATS observations across Kennedy Channel.

In summary, the major conclusions of the analysis are:

1. South of Robeson Channel, the mean current structure depends on the presence or absence of landfast ice. The response is consistent with that imposed by the surface frictional layer, which under landfast ice causes an eastward advection of low-salinity water, a westward shift in the geostrophic current, and a deceleration of near-surface flow. At the CATS mooring line, the current has a subsurface maximum and is offset toward the western sidewall under landfast ice conditions, consistent with observations. When ice free, the surface friction is set by southward winds, which act in the opposite direction of the stress associated with the landfast sea ice.
2. Under landfast ice, temporal variability is controlled by remote forcing, which primarily acts to modulate the amplitude of the mean current structure. In the ocean-only case, the dependence on remote forcing decreases southward through the strait, and at the CATS mooring line, internal dynamics—namely development of an instability with a period of 12–15 days—dominates the variance. The instability is damped the ocean-ice simulation. In addition to the instability, local wind forcing within the strait influences the salinity response in the ocean-only simulation, for which the mode associated with wind forcing represents roughly 20% of the variance at the CATS mooring section and across Smith Sound.
3. The alteration in current structure produces a systematic change in the spatial distribution of salt and heat within the model domain. Low-salinity water is transported midstrait in the ocean-only simulation, and along the eastern boundary in the ocean-ice simulation. The transport of intermediate salinity water is offset to the west in the ice-ocean simulation relative to the ocean-only simulation. Within the ocean-only simulation, intermediate salinity water is also carried northward along the eastern side of the strait. In both simulations, high-salinity water ($S > 34.8$) is constrained to recirculations that are located north and south of a sill in Kane Basin; these recirculations are intensified in the ocean-only simulation.

Differences between the mean structure and variability within the two simulations are notable, and are relevant to our interpretation of seasonal variability within Nares Strait in the current climate as well as ocean

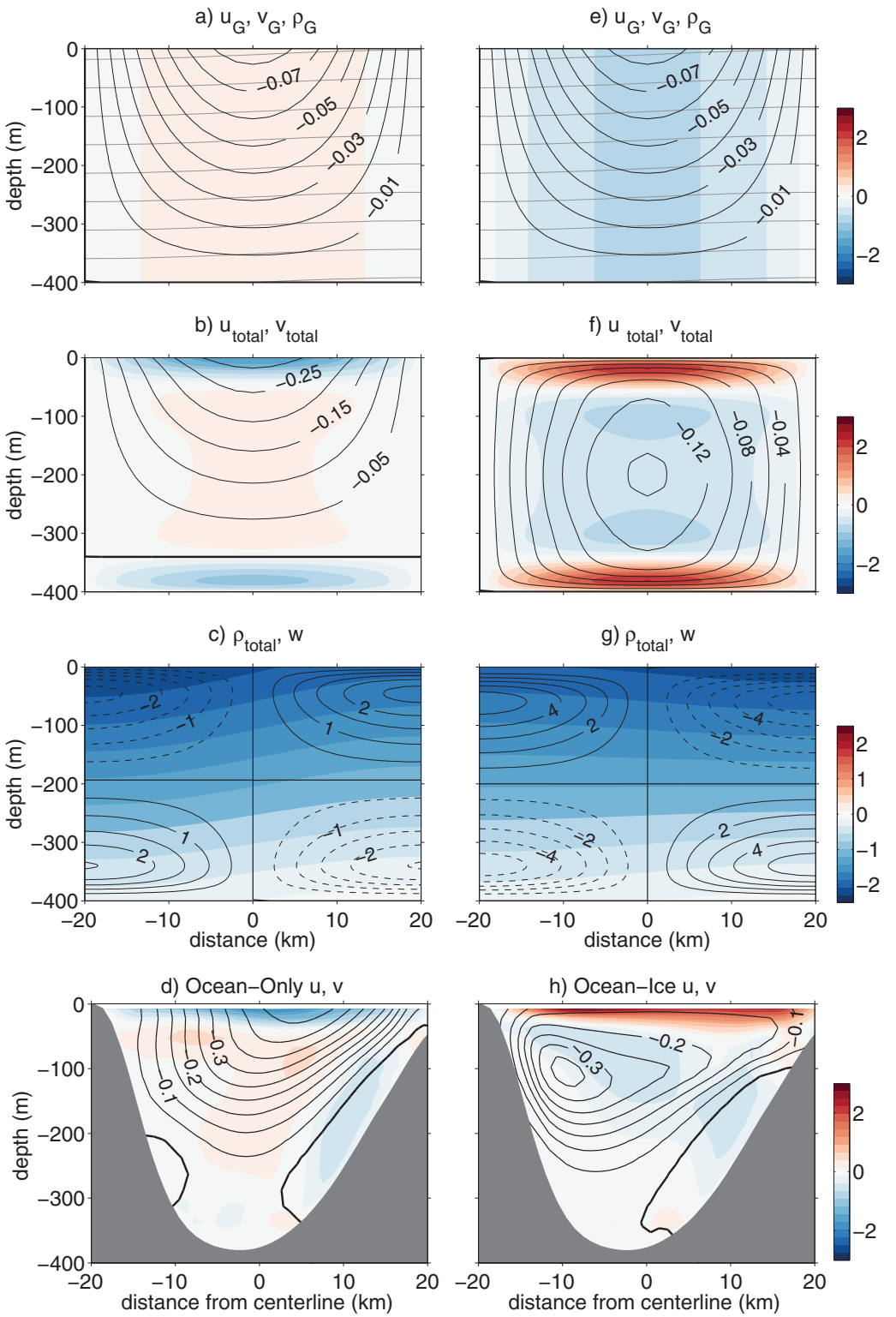

Figure 16. Summary of Ekman-adjustment model for surface (a–c) wind stress and (e–g) ice drag: Figures 16a, 16e show prescribed geostrophic flow with density (gray contours, kg m^{-3}), along-channel velocity (black contours, m s^{-1}), and across-channel velocity (shading, cm s^{-1}). Figures 16b, 16f Ekman-adjusted horizontal velocity fields with along-channel velocity (m s^{-1}) contoured and across-channel velocity (cm s^{-1}) shaded. Figures 16c, 16g Ekman-adjusted density shaded (kg m^{-3}) and vertical velocity (black contours, cm s^{-1}). Figure 16d Ocean-only and Figure 16h ocean-ice numerical model results for annual-mean across-strait (shading) and along-strait (contours) velocity in Kennedy Channel.

circulation in past or future climate scenarios. The sensitivity of mean and time-dependent currents, hydrographic structure, and cross-channel buoyancy transports to the presence or absence of landfast sea ice has implications for the interaction of Nares Strait ocean circulation with the glacial margins of Greenland and Ellesmere Island. For example, the seasonal timing and interannual variability in transports within the strait may affect heat content or circulation modes within glacial fjords and consequently influence the mass loss from the glaciers and ice shelves when present. The time-mean structure of these fields is evidently related to surface frictional characteristics in a qualitatively simple and fundamental way, which emphasizes the importance of properly incorporating factors such as the basal roughness of landfast ice and its representation through ocean-ice drag coefficients in future modeling efforts.

Future projections and paleo reconstructions suggest specific Arctic sea ice condition scenarios for which these results may be relevant and provide useful insight. For example, a shift toward ice-cover consisting of thin, smooth, and more mobile first-year ice—which might be anticipated as Arctic multiyear ice continues to decrease—might extend the seasonal period for which our ocean-only simulation is representative. Conversely, the paleostate of northern Baffin Bay and Nares Strait, after the collapse of the Laurentide Ice Sheet but before the peak warmth of the early Holocene, may have been characterized by permanent landfast ice that would presumably have damped flow features such as the modeled eddy fluctuations, and consequently also reduced cross-strait exchange of heat or salt into Greenland fjords. An intriguing possibility is that the systematic and evidently robust differences in cross-strait location of the southward flow of low and intermediate salinity waters under mobile and landfast ice conditions may have affected sediment deposition patterns in a manner that could yield sediment-core indicators of paleoclimate sea ice states within Nares Strait. Although highly speculative, such potential impacts and interactions imply that models used to predict past or future states of the glacial margins bordering Nares Strait will need to resolve explicitly or parameterize accurately these small time and space scales of regional ocean variability and their coupling to sea ice within and throughout Nares Strait.

Appendix A: Linearized Ekman Adjustment in a Channel

The semianalytical Ekman adjustment model is formulated using the standard Ekman representation of turbulent mixing by a constant eddy viscosity and diffusivity. The model is also simplified through linearization. Salinity advection is approximated by the vertical advection of the constant mean vertical salinity gradient, while momentum advection and advection of salinity perturbations by the disturbance flow are fully neglected. Turbulent salinity diffusion is applied only to the disturbance salinity. The neglect of the turbulent vertical diffusion of the imposed salinity field is necessary to avoid overconstraining the solution; in the ocean-ice and ocean-only simulations, this diffusion can be balanced by advection of the along-channel salinity gradients, but the latter cannot be represented in the two-dimensional model. The model is forced by an imposed pressure gradient in hydrostatic and geostrophic balance. For convenience, the small along-channel component of the pressure gradient is taken as barotropic, while the baroclinic along-channel geostrophic flow is taken to have a level of no motion at the bottom.

Two different sets of surface boundary conditions are imposed. The first corresponds to an imposed surface wind stress, and is representative of the ocean-only simulation or observed mobile-ice conditions. The second corresponds to a derived surface drag, and is representative of the ocean-ice simulation or observed landfast-ice conditions. The Ekman response to the boundary conditions can be decomposed into a primary contribution that fulfills the top and bottom boundary conditions on the horizontal velocity and a secondary contribution that is associated with the horizontal convergence of the lateral Ekman flow. A solution is assumed for velocity $\mathbf{u} = (u,v,w)$, pressure $p = \rho_0 P$ (with ρ_0 a constant reference density), and salinity S of the form

$$(\mathbf{u}, P, S) = (\mathbf{u}_G, P_G, S_G) + (\mathbf{u}_E, P_E, S_E) + (\mathbf{u}_{E2}, P'_{E2}, S'_{E2}), \tag{A1}$$

where G indicates the imposed geostrophic component, E indicates the primary Ekman-layer solution associated with the top and bottom boundary conditions on horizontal velocity (u, v), and $E2$ indicates the secondary Ekman-layer solution induced by the vertical advection of the constant mean vertical salinity gradient. Axes are chosen with x cross-channel, y along-channel (positive northward), and z vertical ($z = 0$ at ocean surface). The channel is taken to have uniform depth with a bottom at $z = -H$ and vertical sides at $x = \{0, L\}$, at which no-normal-flow conditions are satisfied. The imposed geostrophic pressure P_G has the form

$$P_G = G_0\, y \sin\frac{\pi x}{L} - (z+H) g\beta_S\, \delta S_0 \cos\frac{\pi x}{L} - \frac{1}{2}(z+H)^2 g\beta_S \frac{d\bar{S}}{dz}, \tag{A2}$$

in hydrostatic balance with the imposed salinity field S_G,

$$S_G = -\frac{1}{g\beta_S}\frac{\partial P_G}{\partial z} = (z+H)\frac{d\bar{S}}{dz} + \delta S_0 \cos\frac{\pi x}{L}. \tag{A3}$$

Here G_0 and δS_0, respectively, determine the amplitudes of the along-channel barotropic and cross-channel baroclinic pressure gradients, and $d\bar{S}/dz$ is a constant background vertical salinity gradient; g is the gravitational acceleration and β_S is a haline contraction coefficient. The contribution of the first term in (A2) to the cross-channel pressure gradient can be neglected sufficiently close to the (arbitrary) cross-section position $y = 0$, so that, approximately,

$$\left(\frac{\partial P_G}{\partial x}, \frac{\partial P_G}{\partial y}\right) = \left[\left(\frac{\pi}{L}\right) g\beta_S\, \delta S_0 (z+H), G_0\right] \sin\frac{\pi x}{L}, \tag{A4}$$

and the geostrophic velocities are

$$(u_G, v_G) = \frac{1}{f}\left(-\frac{\partial P_G}{\partial y}, \frac{\partial P_G}{\partial x}\right) = (U_G, V_G) \sin\frac{\pi x}{L}, \tag{A5}$$

where f is the constant Coriolis parameter and

$$(U_G, V_G) = \frac{1}{f}\left[-G_0, \left(\frac{\pi}{L}\right) g\beta_S\, \delta S_0 (z+H)\right]. \tag{A6}$$

The geostrophic flow is nondivergent, so $w_G = 0$.

The primary Ekman layer solution serves to adjust the horizontal velocities to the boundary conditions at the bottom and top surfaces ($z = \{-H, 0\}$). From (A5), the geostrophic velocities at the boundary will be proportional to $\sin(\pi x/L)$, so that

$$(u_E, v_E) = (U_E, V_E) \sin\frac{\pi x}{L}. \tag{A7}$$

The choice $w_E = P_E = S_E = 0$ is made, so that the Ekman vertical velocity and associated salinity advection response is contained in the secondary solution. The equations for (U_E, V_E) then reduce to the classical one-dimensional Ekman layer equations with solution (in complex form)

$$\mathrm{U}_E = U_E(z) + iV_E(z) = C_1 \cosh \alpha z + C_2 \sinh \alpha z, \tag{A8}$$

where $\alpha = (1+i)/\delta_E$, $\delta_E = (2A_v/f)^{1/2}$ is the Ekman depth for viscosity A_v, and C_1 and C_2 are complex constants determined by the boundary conditions.

The secondary Ekman flow is induced by the horizontal convergence $\partial u_E/\partial x$, and results in a set of one-dimensional equations for the secondary vertical structure functions:

$$-fV_{E2} - \frac{\pi}{L} P_{E2} = A_v \frac{d^2 U_{E2}}{dz^2} \tag{A9}$$

$$fU_{E2} = A_v \frac{d^2 V_{E2}}{dz^2} \tag{A10}$$

$$\frac{dP_{E2}}{dz} = -g\beta_S S_{E2} \tag{A11}$$

$$\frac{\pi}{L} U_{E2} + \frac{dW_{E2}}{dz} = -\frac{\pi}{L} U_E \tag{A12}$$

$$W_{E2}\frac{d\bar{S}}{dz} = K_v \frac{d^2 S_{E2}}{dz^2}, \tag{A13}$$

where

$$(u_{E2}, v_{E2}) = (U_{E2}, V_{E2}) \sin\frac{\pi x}{L}, \quad (w_{E2}, P'_{E2}, S'_{E2}) = (W_{E2}, P_{E2}, S_{E2}) \cos\frac{\pi x}{L}. \tag{A14}$$

The top and bottom boundary conditions for the secondary Ekman variables are all homogeneous, because the inhomogeneous parts (which are only on horizontal velocity or surface stress) are satisfied by the primary Ekman variables.

The boundary conditions to be satisfied are as follows:

1. At the top ($z = 0$), for the ocean-only case: stress equal to an imposed wind stress $(\tau^x, \tau^y) = (\tau_0^x, \tau_0^y)\sin(\pi x/L)$, which is defined as positive downward and assumed for convenience to have a $\sin(\pi x/L)$ cross-channel structure:

$$\left(\frac{dU_E}{dz}, \frac{dV_E}{dz}\right) = \frac{1}{\rho_0 A_v}(\tau_0^x, \tau_0^y) - \left(\frac{dU_G}{dz}, \frac{dV_G}{dz}\right), \tag{A15}$$

$$\left(\frac{dU_{E2}}{dz}, \frac{dV_{E2}}{dz}\right) = 0. \tag{A16}$$

2. At the top ($z = 0$), for the ocean-ice case: no-slip is applied to the total (sum of geostrophic and Ekman) horizontal velocity field:

$$(U_E, V_E) = -(U_G, V_G), \qquad (U_{E2}, V_{E2}) = 0. \tag{A17}$$

3. At the top ($z = 0$), for both the ocean-only and ocean-ice cases: no-normal-flow is applied to the vertical velocity; a supplemental boundary condition of no turbulent salinity flux is applied directly to the Ekman salinity component; a derived condition of vanishing second derivative is applied to the Ekman pressure component:

$$W_{E2} = \frac{dS_{E2}}{dz} = \frac{d^2 P_{E2}}{dz^2} = 0. \tag{A18}$$

4. At the bottom ($z = -H$), for both the ocean-only and ocean-ice cases: no-slip is applied to the total velocity; a supplemental boundary condition of no turbulent salinity flux is applied directly to the Ekman salinity component; a derived condition of vanishing second derivative is applied to the Ekman pressure component:

$$(U_E, V_E) = -(U_G, V_G), \qquad (U_{E2}, V_{E2}) = 0, \tag{A19}$$

$$W_{E2} = \frac{dS_{E2}}{dz} = \frac{d^2 P_{E2}}{dz^2} = 0. \tag{A20}$$

The solutions shown in Figure 16 were obtained with the following parameters:

$$H = 400 \text{ m}, \; L = 40 \text{ km}$$

$$f = 1.4\times10^{-4}\,\text{s}^{-1}, \; \rho_0 = 1027\,\text{kg m}^{-3}, \; \beta_S = 0.8\times10^{-3}$$

$$\delta S_0 = -0.05, \; d\bar{S}/dz = -2.5/H, \; A_v = K_v = 0.05\,\text{m}^2\,\text{s}^{-1}$$

Ocean-only:

$$\Delta\eta = -0.022 \text{ m}, \quad \tau^x = 0, \quad \tau^y = -0.134\,\text{N m}^{-2}$$

Ocean-ice:

$$\Delta\eta = 0.05 \text{ m}, \quad \tau^x = \tau^y = 0$$

where the along-channel pressure gradient $G_0 = g\Delta\eta/L_y$, with $L_y = 500$ km.

Acknowledgments

This research was supported by the National Science Foundation, grant ARC-1108463. All model forcing and initialization fields are available online from the specified sources: NRL HYCOM+NCODA (https://hycom.org/), ECMWF (http://www.ecmwf.int/en/research/climate-reanalysis/browse-reanalysis-datasets), and the Canadian Archipelago Throughflow Study (http://www.udel.edu/CATS/). Parameter selection details and set up files for the regional model can be obtained by contacting the corresponding author at eshroyer@coas.oregonstate.edu.

References

Adcroft, A., C. Hill, and J. Marshall (1997), Representation of topography by shaved cells in a height coordinate ocean model, *Mon. Weather Rev.*, *125*(9), 2293–2315.

Aksenov, Y, S. Bacon, A. C. Coward and N. P. Holliday (2010), Polar outflow from the Arctic Ocean: A high resolution model study, *J. Mar. Syst.*, *83*(1–2), 14–37.

Berrisford, P., D. Dee, P. Poli, R. Brugge, K. Fielding, M. Fuentes, P. Kallberg, S. Kobayashi, S. Uppala, and A. Simmons (2011), The era-interim archive version 2.0, *Tech. Rep. 1*, European Centre for Medium Range Weather Forecast (ECMWF), Shinfield Park, Reading.

Beszczynska-Möller, A., R. A. Woodgate, C. Lee, H. Melling, and M. Karcher (2011), A synthesis of exchanges through the main oceanic gateways to the arctic ocean, in The Changing Arctic Ocean: Special Issue on the International Polar Year (2007-2009), *Oceanography*, *24*(3), 82–99.

Cavalieri, D. J., T. Markus, and J. C. Comiso (2014), AMSR-E Aqua Daily I3 12.5 km Brightness Temperature, Sea Ice Concentration, And Snow Depth Polar Grids, version 3, NASA National Snow and Ice Data Center Distributed Active Archive Center, Boulder, Colo., doi:10.5067/AMSR-E/AE SI12.003. [Available at http://nsidc.org/data/docs/daac/ae_si25_25km_tb_and_sea_ice.gd.html.]

Chassignet, E. P., H. E. Hurlburt, O. M. Smedstad, G. R. Halliwell, P. J. Hogan, A. J. Wallcraft, R. Baraille, and R. Bleck (2007), The HYCOM (HYbrid Coordinate Ocean Model) data assimilative system, *J. Mar. Syst.*, *65*(1), 60–83.

Curry, B., C. M. Lee, C. M., B. Petrie, R. E. Moritz, and R. Kwok (2014), Multiyear Volume, Liquid Freshwater, and Sea Ice Transports through Davis Strait, 2004–10, *J. Phys. Oceanogr.*, *44*(4), 1244–1266.

Dumont, D., Y. Gratton, and T. E. Arbetter (2009), Modeling the dynamics of the North Water polynya ice bridge, *J. Phys. Oceanogr.*, *39*(6), 1448–1461.
Enderlin, E. M., I. M. Howat, S. Jeong, M.-J. Noh, J. H. Angelen, and M. R. Broeke (2014), An improved mass budget for the Greenland Ice Sheet, *Geophys. Res. Lett.*, *41*, 866–872, doi:10.1002/2013GL059010.
Hibler, W. D. (1980), Modeling a variable thickness sea ice cover, *Mon. Weather Rev.*, *108*(12), 1943–1973, doi:10.1175/1520-0493(1980)108 < 1943:MAVTSI>2.0.CO;2.
Hunke, E. C., and J. K. Dukowicz (1997), An elastic–viscous–plastic model for sea ice dynamics, *J. Phys. Oceanogr.*, *27*(9), 1849–1867, doi:10.1175/1520-0485(1997)027 < 1849:AEVPMF>2.0.CO;2.
Jackett, D. R., and T. J. McDougall (1995), Minimal adjustment of hydrographic profiles to achieve static stability, *J. Atmos. Oceanic Technol.*, *12*(2), 381–389, doi:10.1175/1520-0426(1995)012 < 0381:MAOHPT>2.0.CO;2.
Jakobsson, M., et al. (2012), The International Bathymetric Chart of the Arctic Ocean (IBCAO) version 3.0, *Geophys. Res. Lett.*, *39*, L12609, doi:10.1029/2012GL052219.
Johnson, H. L., A. Münchow, K. K. Falkner, and H. Melling (2011), Ocean circulation and properties in petermann fjord, greenland, *J. Geophys. Res.*, *116*, C01003, doi:10.1029/2010JC006519.
Kliem, N. and D. A. Greenberg (2003), Diagnostic simulations of the sumer circulation in the Canadian arctic archipelago, *Atmos. Ocean*, *41*(4), 273–289.
Kwok, R. (2005), Variability of Nares Strait ice flux, *Geophys. Res. Lett.*, *32*, L24502, doi:10.1029/2005GL024768.
Kwok, R., L. Toudal Pedersen, P. Gudmandsen, and S. S. Pang (2010), Large sea ice outflow into the Nares Strait in 2007, *Geophys. Res. Lett.*, *37*, L03502, doi:10.1029/2009GL041872.
Large, W. G., and S. Pond (1981), Open ocean momentum flux measurements in moderate to strong winds, *J. Phys. Oceanogr.*, *11*(3), 324–336, doi:10.1175/1520-0485(1981)011 < 0324:OOMFMI>2.0.CO;2.
Large, W. G., J. C. McWilliams, and S. C. Doney (1994), Oceanic vertical mixing: A review and a model with a nonlocal boundary layer parameterization, *Rev. Geophys.*, *32*, 363–404, doi:10.1029/94RG01872.
Lique, C., A.-M. Treguier, M. Scheinert, and T. Penduff (2009), A model-based study of ice and freshwater transport variability along both sides of Greenland, *Clim. Dyn.*, *33*, 685–705, doi:10.1007/s00382-008-0510-7.
Losch, M., D. Menemenlis, J.-M. Campin, P. Heimbach, and C. Hill (2010), On the formulation of sea-ice models. part 1: Effects of different solver implementations and parameterizations, *Ocean Modell.*, *33*(1–2), 129–144, doi:10.1016/j.ocemod.2009.12.008.
Lu, Y., S. Higginson, S. Nudds, S. Prinsenberg, and G. Garric (2014), Model simulated volume fluxes through the Canadian Arctic Archipelago and Davis Strait: Linking monthly variations to forcing in different seasons, *J. Geophys. Res. Oceans*, *119*, 1927–1942, doi:10.1002/2013JC009408.
Marshall, J., A. Adcroft, C. Hill, L. Perelman, and C. Heisey (1997), A finite-volume, incompressible Navier Stokes model for studies of the ocean on parallel computers, *J. Geophys. Res.*, *102*, 5753–5766, doi:10.1029/96JC02775.
McGeehan, T. and W. Maslowski (2012), Evaluation and control mechanisms of volume and freshwater export through the Canadian Arctic Archipelago in a high-resolution pan-Arctic ice-ocean model, *J. Geophys. Res.*, *117*, C00D14, doi:10.1029/2011JC007261.
Metzger, E. J., O. M. Smedstad, P. G. Thoppil, H. E. Hurlburt, J. A. Cummings, A. J. Wallcraft, L. Zamudio, D. S. Franklin, P. G. Posey, and M. W. Phelps (2014), US Navy operational global ocean and arctic ice prediction systems, *Oceanography*, *27*(3), 32–43, doi:10.5670/oceanog.2014.66.
Münchow, A. (2015), Volume and freshwater flux to the West of Greenland: Nares Strait 2003-09, *J. Phys. Oceanogr.*, doi:10.1175/JPO-D-15-0093.1, in press.
Münchow, A., and H. Melling (2008), Ocean current observations from Nares Strait to the west of Greenland: Interannual to tidal variability and forcing, *J. Mar. Res.*, *66*(6), 801–833.
Münchow, A., H. Melling, and K. K. Falkner (2006), An observational estimate of volume and freshwater flux leaving the Arctic Ocean through Nares Strait, *J. Phys. Oceanogr.*, *36*, 2025–2041.
Rabe, B., A. Münchow, H. L. Johnson, and H. Melling (2010), Nares Strait hydrography and salinity field from a 3-year moored array, *J. Geophys. Res.*, *115*, C07010, doi:10.1029/2009JC005966.
Rabe, B., H. L. Johnson, A. Münchow, and H. Melling (2012), Geostrophic ocean currents and freshwater fluxes across the Canadian polar shelf via Nares Strait, *J. Mar. Res.*, *70*(4), 603–640.
Rasmussen, T. A., N. Kliem, and E. Kaas (2010), Modelling the sea ice in the Nares Strait, *Ocean Modell.*, *35*(3), 161–172 1463–5003.
Rignot, E., I. Fenty, D. Menemenlis, and Y. Xu (2012), Spreading of warm ocean waters around Greenland as a possible cause for glacier acceleration, *Ann. Glaciol.*, *53*(60), 257–266.
Samelson, R. M., and P. L. Barbour (2008), Low-level jets, orographic effects, and extreme events in Nares Strait: A model-based mesoscale climatology, *Mon. Weather Rev.*, *136*(12), 4746–4759, doi:10.1175/2007MWR2326.1.
Semtner, A. J. (1976), A model for the thermodynamic growth of sea ice in numerical investigations of climate, *J. Phys. Oceanogr.*, *6*(3), 379–389, doi:10.1175/1520-0485(1976)006 < 0379:AMFTTG>2.0.CO;2.
Straneo, F., and P. Heimbach (2013), North Atlantic warming and the retreat of Greenland's outlet glaciers, *Nature*, *504*, 36–43.
Wekerle, C., Q. Wang, S. Danilov, T. Jung, and J. Schröter (2013), The Canadian Arctic Archipelago throughflow in a multiresolution global model: Model assessment and the driving mechanism of interannual variability, *J. Geophys. Res. Oceans*, *118*, 4525–4541, doi:10.1002/jgrc.20330.
Zhang, J., W. D. Hibler, M. Steele, and D. A. Rothrock (1998), Arctic ice–ocean modeling with and without climate restoring, *J. Phys. Oceanogr.*, *28*(2), 191–217, doi:10.1175/1520-0485(1998)028 < 0191:AIOMWA>2.0.CO;2.